Time-correlated Background and Background Mitigation Strategies in the KATRIN Experiment

Master thesis at the faculty of physics
of the
Ludwig-Maximilians-Universität München

submitted by
Alessandro Schwemmer
born in Neustadt an der Waldnaab

Munich, 13.10.2020

Supervisor (LMU): Prof. Dr. Thomas Kuhr
Supervisor (MPP): Prof. Dr. Susanne Mertens

LMU LUDWIG-MAXIMILIANS-UNIVERSITÄT MÜNCHEN

MAX-PLANCK-INSTITUT FÜR PHYSIK

Zeitlich korrelierter Untergrund und Strategien zur Untergrunddunterdrückung im KATRIN Experiment

Masterarbeit an der Fakultät für Physik
der
Ludwig-Maximilians-Universität München

vorgelegt von
Alessandro Schwemmer
geboren in Neustadt an der Waldnaab

München, den 13.10.2020

Betreuer (LMU): Prof. Dr. Thomas Kuhr
Betreuerin (MPP): Prof. Dr. Susanne Mertens

Abstract

The Karlsruhe Tritium Neutrino (KATRIN) experiment aims at measuring the neutrino mass with a sensitivity of 0.2 eV (90 % C.L.) in a model independent way. To this end it uses electrons originating from tritium β-decay and investigates their spectrum close to the kinematic endpoint. In order to reach the desired sensitivity a low background and a good understanding of its properties is necessary. This thesis presents a data-driven Monte Carlo simulation of the background focusing on its non-Poissonian nature which originates from nuclear decays in the main spectrometer. The impact of a non-Poisson background on the neutrino mass under various model assumptions and measurement configurations is investigated. It could be shown that different scanning strategies and background treatments have a minor impact on the neutrino mass result. Furthermore optimising the electromagnetic field configuration in the main spectrometer allows for an overall background reduction by a factor of 2. However this asymmetric setting requires precise measurements of the electromagnetic fields in the center of the spectrometer. In the scope of this thesis a new method of field calibrations with a gaseous krypton source has been established and the field input values for the third neutrino mass campaign were provided.

Zusammenfassung

Das Ziel des Karlsruhe Tritium Neutrino (KATRIN) Experiments ist die Messung der Neutrinomasse mit einer Sensitivität von 0.2 eV (90 % C.L.) in einer modelunabhängigen Art und Weise. Dazu nutzt es Elektronen aus dem Tritium β-Zerfall und untersucht deren Spektrum nahe des kinematischen Endpunkts. Um die gewünschte Sensitivität zu erreichen, ist ein niedriger Untergrund sowie dessen gutes Verständnis notwendig. Diese Arbeit stellt eine auf Daten basierte Monte Carlo Simulation des Untergrunds vor und konzentriert sich dabei auf dessen Abweichung von einer Poisson Verteilung, was seinen Ursprung in Kernzerfällen im Hauptspektrometer hat. Die Auswirkung dieses non-Poisson Untergrunds auf die Neutrinomasse wurde unter verschiedenen Modellannahmen und Messkonfigurationen untersucht. Es zeigte sich, dass unterschiedliche Scanstrategien und Untergrundbehandlungen zu einer kleinen Auswirkung auf die Neutrinomasse führen. Weiterhin erlaubt eine Optimierung der elektromagnetischen Felder im Hauptspektrometer die Reduzierung des totalen Untergrunds um einen Faktor 2. Diese asymmetrische Konfiguration erfordert jedoch präzise Messungen der elektromagnetischen Felder im Spektrometer. Im Rahmen dieser Arbeit wurde eine neue Methode zur Feldkalibrierung mit einer gasförmigen Kryptonquelle herangezogen und Feldwerte für die dritte Messung der Neutrinomasse wurden angegeben.

Contents

Chapter 1

The neutrino

Despite being one of the most abundant particles in the universe, there are still open questions concerning the neutrino. Due to its weak interactions with other particles and its small mass, it took many years from its prediction to evidence of its existence. And still today the neutrino offers room for discussion. This chapter describes briefly the neutrino's history, its description in the standard model (SM) of particle physics and the implications of neutrino oscillations on the SM. For better readability this thesis uses natural units ($\hbar = c = 1$).

1.1 History of discovery

The motivation for the neutrino was coming from J. Chadwick's investigations of the β-spectrum in the early 20^{th} century. As α and γ-spectra showed discrete lines representing the energy difference between the nuclei, the continuous β-spectrum was not understood in the first place [1]. At this time, the β-decay was thought to be a two-body-decay: The nucleus emits an electron e^- and a proton p, their energy is dictated by energy-momentum-conservation, i. e. the spectrum should be discrete.
This discrepancy between theory and experiment lead W. Pauli to the proposal of a new particle, now known as the neutrino ν. As charge is conserved, this particle should be neutral, but not a photon as this could be easily detected [2].
Building up on the idea of this postulated particle, E. Fermi formulated his theory of β-decay: A neutron n in the nucleus decays into a proton, an electron and a (anti-)neutrino $\bar{\nu}$ (see eq. (1.1)). In this three-body-decay, the individual energies of the particles in the final state are not fixed, therefore the spectrum is continuous [3].

$$n \to p + e^- + \bar{\nu}_e \tag{1.1}$$

Between the theoretical postulate of the neutrino and its discovery over 20 years passed. The conformation took place in 1956, done by C. L. Cowan and F. Reines. They used a nuclear fission reactor as (potential) neutrino source. Those neutrinos reacted with protons in a target tank, producing positrons and neutrons, see eq. (1.2). In this case, the signal consists two energy depositions. The prompt one being two γ photons originating from the annihilation of the positron e^+. The delayed energy deposition is caused by cadmium capturing the neutron n and releasing a γ photon (see e.g. eq. (1.3)). A signal to background ration of 3 to 1 and signal dependence on the reactor power lead to the conclusion that the signal is indeed induced by a neutrino [4, 5].

$$\nu_e + p \to n + e^+ \tag{1.2}$$

$$^{113}\text{Cd} + n \to {}^{114}\text{Cd} + \gamma\,(9.2\,\text{MeV}) \tag{1.3}$$

1.2 Description in the standard model of particle physics

The standard model (SM) of particle physics describes all known particles and interactions with high precision. It characterises the neutrino as a massless, uncharged lepton. Interactions between the neutrino and other particles are mediated via the weak force. This only involves left-handed neutrinos. Right-handed neutrinos either do not exist or interact exclusively via gravitation. In the framework of electroweak theory, left-handed leptons are grouped in doublets in accordance with their (weak) isospin as shown in eq. (1.4) for the three generations. As right-handed leptons do not interact via charged currents[1] and hence have no isospin, they form singlets as given in eq. (1.5). A very similar procedure holds for quarks, but is not presented here. Therefore the electroweak interaction affects all fermions [6].

$$\begin{pmatrix} \nu_e \\ e^- \end{pmatrix}_{\mathrm{L}}, \begin{pmatrix} \nu_\mu \\ \mu^- \end{pmatrix}_{\mathrm{L}}, \begin{pmatrix} \nu_\tau \\ \tau^- \end{pmatrix}_{\mathrm{L}} \tag{1.4}$$

$$e^-_{\mathrm{R}}, \mu^-_{\mathrm{R}}, \tau^-_{\mathrm{R}} \tag{1.5}$$

Charged currents are described by massive gauge bosons denoted as $W^\pm$. As their mass is $\mathcal{O}(80\,\mathrm{GeV})$ Fermi's theory that does not include these bosons is valid at low energies in which case the interaction is reduced to a single point. An example of a possible interaction is shown in fig. 1.1, the handedness is not shown explicitly.

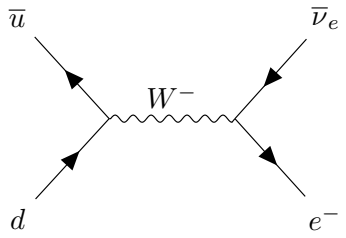

Figure 1.1: Example of a charged current.

Furthermore leptons obey another conservation law. Each lepton is assigned a lepton number, being 1 or -1 for particles or anti-particles respectively. This number is conserved globally and in particular for each individual generation. Violations of this number have so far only observed in the context of neutrino oscillations. This will be explored in the next section [7].

1.3 Neutrino oscillations and their implications

In 1968, R. Davis Jr. conducted his famous Homestake experiment to search for neutrinos from the sun: A tank filled which liquid tetrachloroethylene served as the detector. Incoming electron neutrinos react with the chlorine and produce argon, together with an electron (eq. (1.6)). The produced argon is removed from the tank and its decays allow for an estimation of the previous production, hence for the ν_e flux. The observed flux coming from the sun is significantly smaller than expected from theoretical predictions [8]. This marks the first hint to neutrino oscillations.

$$^{37}\mathrm{Cl} + \nu_e \rightarrow {}^{37}\mathrm{Ar} + e^- \tag{1.6}$$

[1] As the distinction suggests there are also neutral currents, which are not covered here. Please refer to [6].

In the following years various experiments have shown flavour changes of neutrinos travelling over large distances. Looking at atmospheric neutrinos induced by cosmic rays have shown evidence for neutrino oscillations, in good agreement with the two-flavour oscillation hypothesis, see eq. (1.7). In this simplified model, the probability for a neutrino ν_a to oscillate and be observed in a different flavor state ν_b after travelling a distance L depends on its energy E_ν, the mixing angle θ and the mass squared difference Δm^2 [9].

$$P(\nu_a \to \nu_b) = \sin^2(2\theta) \cdot \sin^2\left(\frac{1.27\Delta m^2(\mathrm{eV}^2)L(\mathrm{km})}{E_\nu(\mathrm{GeV})}\right) \tag{1.7}$$

Since the oscillations would disappear for vanishing Δm^2, this implies that not all neutrinos can be massless. As described in section 1.2, there are three generations, i.e. three flavors of neutrinos. In general oscillations between every pair of them are possible. To account for their masses, three mass eigenstates ν_i, $i \in \{1, 2, 3\}$ are introduced which mix with the weak eigenstates ν_l, $l \in \{e, \mu, \tau\}$, see eq. (1.8). The strength of the mixing is parametrised by the matrix elements U_{li} [7, 10].

$$|\nu_l\rangle = \sum_i U_{li} \, |\nu_i\rangle \tag{1.8}$$

However neutrino oscillations are only sensitive to mass squared differences. For a direct neutrino mass measurement, a different type of experiment is needed. This is described in the following section.

Chapter 2

The KATRIN Experiment

The Karlsruhe Tritium Neutrino (KATRIN) experiment aims at measuring the neutrino mass in a direct, model independent fashion. Similar to its predecessors in Mainz [11] and Troitsk [12], its observable is the effective anti-neutrino mass $m(\nu_e)$:

$$m(\nu_e) = \sqrt{\sum_{i=1}^{3} |U_{ei}|^2 m_i^2} \tag{2.1}$$

After three years of data taking, KATRIN is designed to have a sensitivity of $m(\nu_e) \equiv m_\nu = 0.2\,\mathrm{eV}$ at 90 % confidence level (C.L.) [13].
Section 2.1 gives an overview of the tritium β-decay used for the neutrino mass determination, followed by a short description of the measurement principle in section 2.2. The model of the integral tritium spectrum is given in section 2.3 while the data modelling tool is presented in section 2.4. A short experimental overview is presented in section 2.5. This chapter is concluded with results from the first neutrino mass measurement campaign in section 2.6.

2.1 Tritium β-decay

In order to measure the neutrino mass m_ν as defined in eq. (2.1), KATRIN uses electrons coming from the β-decay of Tritium:

$$^3\mathrm{H} \rightarrow {}^3\mathrm{He}^+ + e^- + \bar{\nu}_e \tag{2.2}$$

The neutrino mass would manifest itself in a distortion of the spectrum (see fig. 2.1), which would be visible mostly near the endpoint E_0, the maximal energy of an electron assuming $m_\nu = 0\,\mathrm{eV}$ [13]. The differential decay rate of tritium can be described using Fermi's Golden Rule. One obtains eq. (2.3). $F(Z,E)$ represents the Fermi function describing Coulomb interaction between the electron and the nucleus in the final state having an atomic charge Z. E, p and m_e refer to energy, momentum and mass of the electron respectively while Θ is the Heaviside function guaranteeing energy conservation. The constant C' is given in terms of the Fermi constant G_F, the Cabibbo angle θ_C and the nuclear transition matrix element M_nuc (see eq. (2.4)) [14, 15].

$$\frac{\mathrm{d}\Gamma}{\mathrm{d}E} = C' \cdot F(Z,E) \cdot p \cdot (E + m_e) \cdot (E_0 - E) \cdot \sqrt{(E_0 - E)^2 - m_\nu^2} \cdot \Theta(E_0 - E - m_\nu) \tag{2.3}$$

$$C' = \frac{G_\mathrm{F}^2 \cos\theta_\mathrm{C}{}^2}{2\pi^2} \cdot |M_\mathrm{nuc}|^2 \tag{2.4}$$

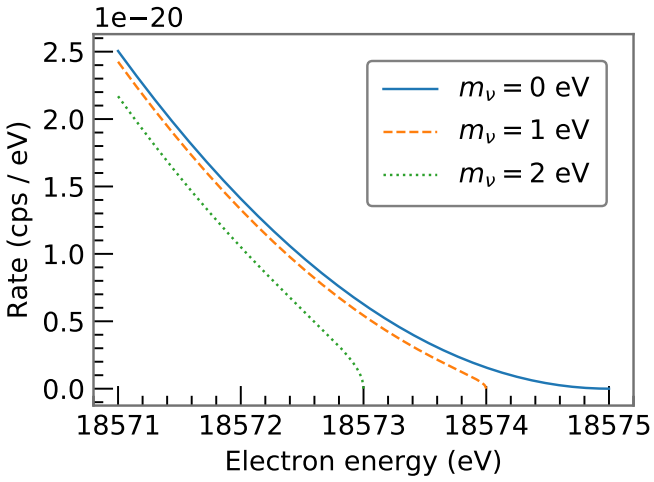

Figure 2.1: Effect of m_ν on the tritium spectrum near E_0 [14].

For a precise modelling, further modifications of the differential spectrum become necessary. This includes but is not limited to the thermal induced Doppler effect or the distribution of molecular final states, see [14, 15].

2.2 MAC-E filter

Following the success of the Mainz and Troitsk neutrino mass experiments, KATRIN uses a magnetic adiabatic collimation combined with an electrostatic filter (MAC-E filter) in its spectrometers. This filter combines the needed high energy resolution with high luminosity [13].
The β-electrons coming from the source are guided by magnetic field lines through the spectrometer, as sketched in fig. 2.2. On their way they perform cyclotron motion around the field lines, resulting in an acceptance angle of up to 2π. Due to the magnetic mirror effect this angle however is limited and usually around 50° in KATRIN [13].
As the electrons move through the spectrometer the B-field drops by several orders of magnitude until it reaches its minimum B_{min}, defining the analysing plane (AP). Because of the gradient in the magnetic field, cyclotron motion is converted into longitudinal motion, shown in the bottom of fig. 2.2 [13].
The electric potential is maximal in the AP, thus this conversion of longitudinal electron momentum enables electrons that start with an non-zero pitch angle θ w.r.t. the magnetic field lines to overcome the potential barrier, despite having not enough longitudinal energy in the first place.
Altogether this filter acts as an integrating high-energy pass filter with its energy resolution being determined solely by the magnetic fields:

$$\frac{\Delta E}{E} = \frac{B_{\text{min}}}{B_{\text{max}}} \tag{2.5}$$

with B_{min} and B_{max} being the minimal and maximal magnetic field respectively [13].

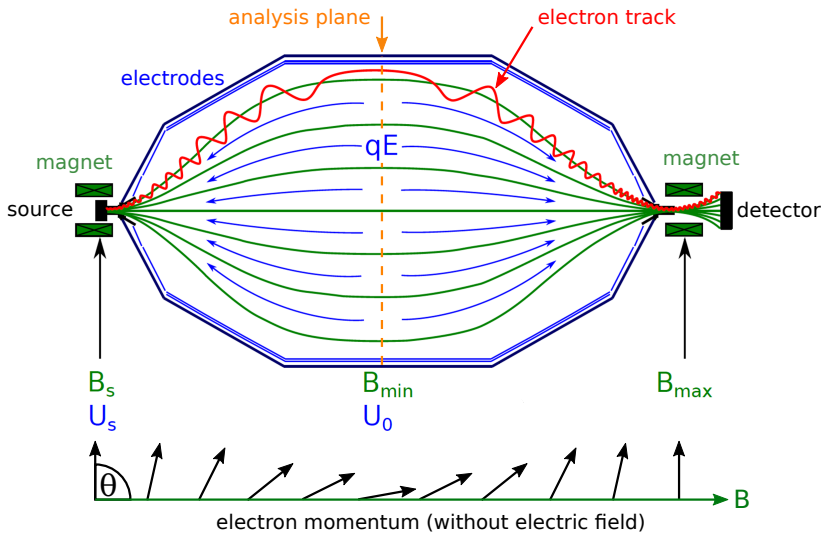

Figure 2.2: Top: Sketch of a MAC-E filter. Electrons (red) coming from the source are adiabatically guided through the spectrometer, performing cyclotron motion along the magnetic field lines (green). If their energy is high enough to surpass the potential barrier introduced by the electrodes (blue), the electrons are re-accelerated towards the detector as they passed the analysing plane (AP) (orange dashed), where the electric potential is maximal and the magnetic field is minimal. Bottom: Because of the magnetic field gradient, the electrons cyclotron motion is converted into longitudinal motion while approaching the AP [16].

2.3 Model of the integral β-spectrum

The integral β-decay spectrum consists of multiple parts. The differential spectrum given in section 2.1 is combined with the experimental response of KATRIN presented in section 2.3.1. Subsequently additional modifications to account for background, thermal Doppler broadening and other effects are applied (see section 2.3.2).

2.3.1 Response function

As described in the previous section, KATRIN uses a MAC-E filter, resulting in an integrating high-energy pass filter. Therefore only electrons having sufficient (longitudinal) energy can reach the detector. This property is encoded in the response function $R(qU, E)$ which gives the probability for an electron with energy E to pass the MAC-E filter with fixed retarding energy qU. Ideally, this would be a simple step function as given in eq. (2.6) [14].

$$R_{\text{ideal}}(qU, E) = \begin{cases} 0, & \text{if } E < qU \\ 1, & \text{if } E \geq qU \end{cases} \tag{2.6}$$

However the MAC-E filter does not convert all transversal energy into longitudinal energy. Therefore even electrons with a total energy larger than the retarding energy may not overcome the potential barrier. Following eq. (2.5) a normalized relativistic transmission $T(qU, E)$ function can be derived, describing the electron transmission probability:

$$T(qU, E) = \begin{cases} 0, & \text{if } E < qU \\ \dfrac{1-\sqrt{1-f\cdot\frac{B_S}{B_{\min}}\cdot\frac{E-qU}{E}}}{1-\sqrt{1-\frac{B_S}{B_{\max}}}}, & \text{if } qU \leq E \leq qU\frac{f\cdot B_{\max}}{f\cdot B_{\max}-B_{\min}} \\ 1, & \text{if } E > qU\frac{f\cdot B_{\max}}{f\cdot B_{\max}-B_{\min}} \end{cases} \tag{2.7}$$

with q being the electric charge of the particle, E its total energy, qU the retarding energy and f a relativistic factor given by eq. (2.8) [14]. The shape of the transmission is shown in fig. 2.3a. For $B_{\text{min}} = 0$, the transmission would resemble a simple step function like for an ideal high-pass energy filter.

$$f = \frac{\frac{E-qU}{m_e} + 2}{\frac{E}{m_e} + 2} \tag{2.8}$$

Due to scattering of electrons with tritium molecules in the source the transmission function has to be modified. To this end the energy loss in each scattering process is included by convolving the transmission with the corresponding scattering probabilities and their energy loss function. Thus one obtains the KATRIN response function $R(qU, E)$, shown in fig. 2.3b [14].

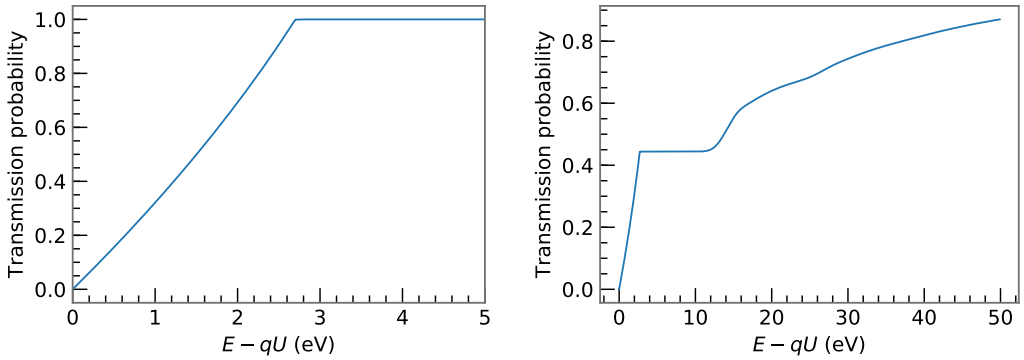

(a) Transmission (b) Response

Figure 2.3: Transmission probability and response function. The latter includes scattering of electrons in the source [14].

2.3.2 Integral spectrum

Combining the previously discussed response function $R(qU, E)$ and the differential decay spectrum $\frac{\mathrm{d}\Gamma}{\mathrm{d}E}(E)$ from section 2.1 gives the integral spectrum $I(qU)$ of KATRIN. It is calculated via a convolution as given in eq. (2.9). Additionally a constant background rate B is added. The number of tritium atoms N_{eff}, the acceptance angle θ_{max} and the detection efficiency $\epsilon_{\text{detector}}$ are absorbed in C (see eq. (2.10)). Details are given in [14].

$$\Gamma(qU) = I(qU) + B = C \cdot \int_{qU}^{E_0} \frac{\mathrm{d}\Gamma}{\mathrm{d}E}(E) \cdot R(qU, E)\,\mathrm{d}E + B \tag{2.9}$$

$$C = N_{\text{eff}} \cdot \frac{1 - \cos\theta_{\text{max}}}{2} \cdot \epsilon_{\text{detector}} \tag{2.10}$$

2.4 Fitrium software

Fitting and modelling the data obtained in KATRIN is done using Fitrium. It includes, amongst others, the (integral) tritium model described in section 2.3 and a model for conversion electrons from krypton (see section 5.2.1). Currently Fitrium is maintained and developed by Christian Karl and Martin Slezák. It offers the capability to fit a spectrum, but also to perform Monte Carlo (MC) simulations and to propagate systematic uncertainties [14].

Fitting a spectrum is done via a maximum likelihood analysis. To this end, a likelihood function $\mathcal{L}$ is defined:

$$\mathcal{L} = \mathcal{L}(\mu(\vec{\theta}); x) = \mathcal{L}(\vec{\theta}; x) \tag{2.11}$$

This likelihood function describes the probability for a model μ with parameters $\vec{\theta}$ to be realised given the data from experiment x. It is maximised by finding the optimal parameters decoded in $\vec{\theta}$ to describe the data. To this end the negative logarithmic likelihood is minimised, which is given in eq. (2.12) and related to the χ^2 (defined in eq. (2.13)) for Gaussian distributed data [14].

$$-\ln \mathcal{L}(\mu; x) = \frac{1}{2}\chi^2(\mu; x) \tag{2.12}$$

$$\chi^2(\mu; x) = \sum_i \frac{(x_i - \mu_i)^2}{\sigma_i^2} \tag{2.13}$$

Here x_i denotes the data points that are compared to their model expectation μ_i and weighted by their uncertainty σ_i.
Systematic uncertainties like the magnetic fields can easily be included by modifying the likelihood function with a pull-term (also called nuisance parameter). Typically this means a multiplication with a Gaussian (see appendix B.2) that constrains the systematic parameter in terms of its expectation value and uncertainty. However this leads to increased computational effort as the systematic parameter is an additional parameter that needs to be optimised [14].
A different approach is to use covariance matrices. In this case the χ^2 is defined to be

$$\chi^2(\mu; x) = (\mu - x)^\intercal V^{-1} (\mu - x) \tag{2.14}$$

with V being the covariance matrix. In addition to statistical uncertainties, systematics are included by calculating multiple model spectra sampling the systematic parameters from their distribution. The covariance matrix is then calculated from these model spectra.
A third possibility is to repeat the fit instead of calculating a model spectrum. This is done in the framework of MC propagation and leads to a distribution of the fit parameter(s) which is broadened w.r.t. a statistics only case. For a detailed discussion of the fitting procedure and the treatment of systematic uncertainties, please refer to [14].

2.5 Experimental overview

The length of the KATRIN experiment is 70 m. Its beamline, shown in fig. 2.4, unifies different components described in the following. Each part serves a different, unique purpose.

2.5.1 Rear Section

The rear section mainly serves as a calibration and monitoring system. It consists of a gold-plated stainless-steel disk with a central aperture of 5 mm, allowing to sent electrons or ions through the beamline. As the electrons are coming from a photo-electronic source, their energy and pitch angle w.r.t. the magnetic field is well defined, thus allowing for measurement of the response function (see section 2.3.1) and other systematic effects. The rear wall (RW) itself can be used to characterise the plasma and avoid distortions of the spectrum induced by additional potentials [17, 18].

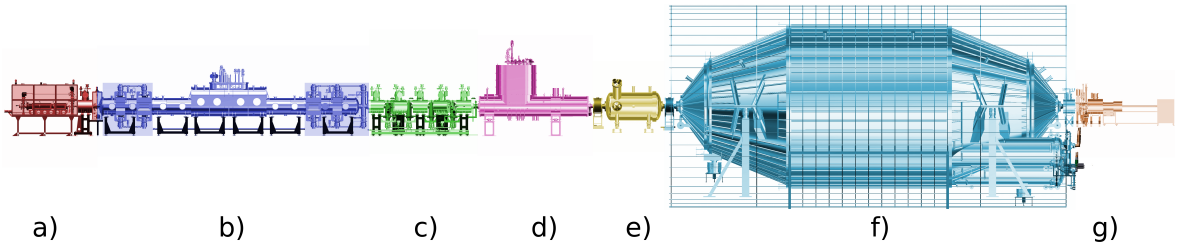

Figure 2.4: KATRIN beamline:
a) Rear section
b) Windowless gaseous tritium source (WGTS)
c) Differential pumping section (DPS)
d) Cryogenic pumping section (CPS)
e) Pre-spectrometer (PS)
f) Main spectrometer (MS)
g) Focal plane detector (FPD)

2.5.2 Windowless Gaseous Tritium Source

The 10 m long windowless gaseous tritium source (WGTS) houses the tritium molecules delivering up to 10^{11} β-decay electrons per second as long as KATRIN is operating in usual tritium mode. The gas is cooled down as low as 27 K and has a high isotopic purity ($> 95\,\%$). It is inserted through a set of capillaries in the middle. By controlling the gas injection pressure, the column density ρd of the WGTS can be adjusted w.r.t. its reference value of $5 \times 10^{17}\,\mathrm{cm}^{-2}$. The produced electrons are adiabatically guided through the source using a magnetic field B_S until reaching the end of the tube [13].

2.5.3 Transport Section

As the β-electrons reach the end of the WGTS tube they are supposed to enter the spectrometer. In order to avoid tritium doing so as well, leading to elevated spectrometer background, the transport section consists of the differential pumping section (DPS) and the cryogenic pumping section (CPS).
The DPS uses turbomolecular pumps in order to reduce the gas-flow by at least five orders of magnitudes. The electrons are guided adiabatically through this section, while neutral molecules hit the beamtube which is composed of tilted neighbouring elements. Tritium-containing ions are removed using a ring electrode and electric dipole elements.
Subsequently the CPS reduces the tritium flow by additional seven orders of magnitude using cold traps. Similar to the DPS tritium molecules strike the wall due to a tilt of beamtube segments. As the wall consists of a 3 K argon-frost layer which provides a higher binding energy than normal cryo-condensation, tritium molecules are adsorbed.
After passing this section, the electrons may enter the spectrometer while the gas-flow has been reduced by about 10^{12} [18].

2.5.4 Pre- and Main Spectrometer

Both spectrometers are based on a MAC-E filter as described in section 2.2. The PS is operated at fixed retarding potential, thus acting as a pre-filter. This minimises background coming from ionization of residual gas molecules in the MS. The MS itself scans the β-spectrum using different retarding energies close to the endpoint E_0. To suppress the background

further, it has an inner electrode (IE) at slightly more negative potential. This way low-energy electrons or ions emanating from the inner surface of the vessel may not enter the flux tube. To avoid scattering on residual gas, the pressure in the pre- and main spectrometer is only 1×10^{-11} mbar [13].

2.5.5 Focal plane detector

The FPD completes the KATRIN beamline. It is a multi-pixel silicon diode array, segmented in 148 pixels as shown in fig. 2.5. All pixels have the same surface area. Electrons coming from the MS are accelerated by 10 kV using a post-acceleration electrode (PAE). This PAE allows for additional background reduction, induced by for instance β- and γ-emitting nuclei close to the detector [13, 18].

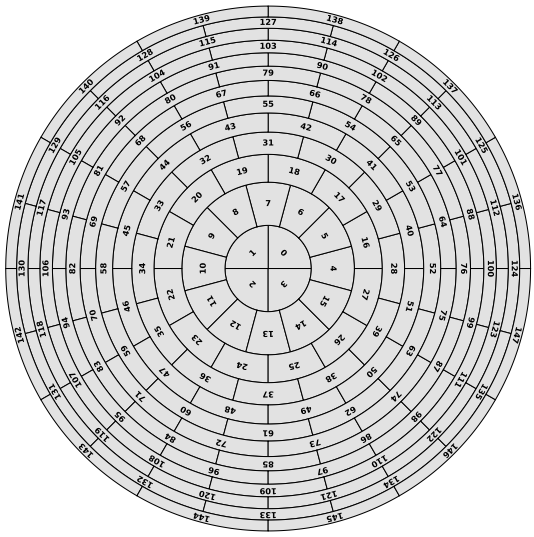

Figure 2.5: Segmentation of the focal plane detector. The pixels are labelled counter-clockwise from inside to the outside.

2.6 First neutrino mass measurement campaign

The first neutrino mass measurement campaign called KATRIN neutrino mass 1 (KNM1) took place in spring 2019. The integral tritium β-decay spectrum is scanned multiple times. Each scan lasts about 2 h and consists of various subscans at different retarding energies qU. For one subscan the retarding energy is fixed and electrons reaching the detector are counted for a certain amount of time. The spent time for each retarding potential is higher in the region close to the tritium endpoint E_0 as the distortion due to m_ν is maximal there (see fig. 2.6 c) [19].
In total 274 scans are selected based on data quality criteria. Those scans are then stacked at $\langle qU \rangle$ for each subscan. For further analysis, noisy and shadowed pixels are excluded and 117 pixels are used when fitting the data. The corresponding spectrum and the best-fit model are

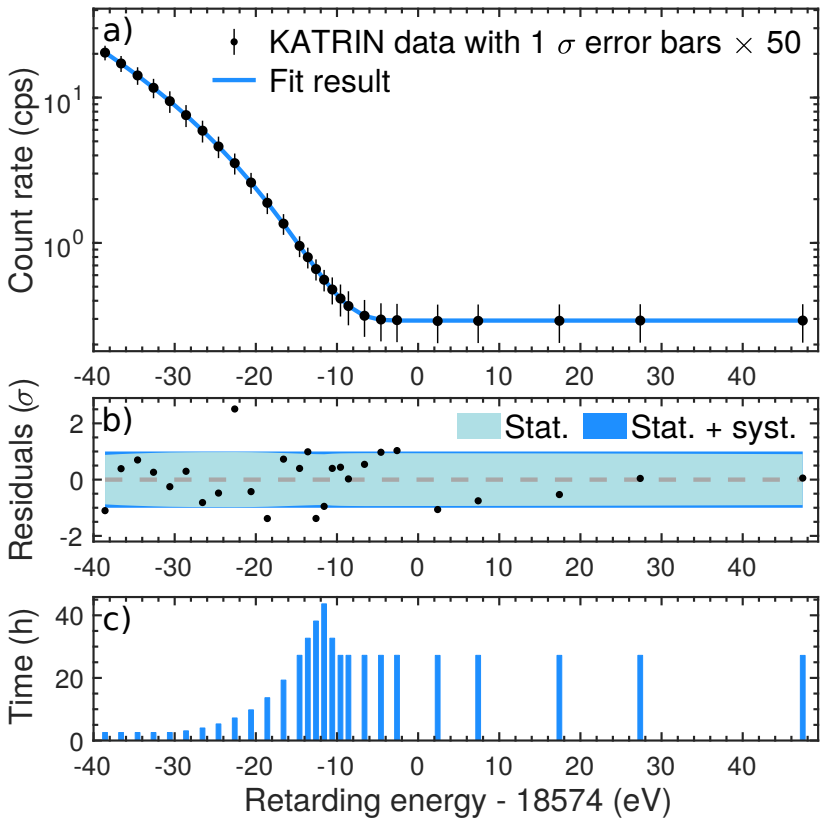

Figure 2.6: a) Integral spectrum of electrons after stacking 274 scans. The uncertainties are enlarged by a factor of 50. The best-fit model is also shown. b) Residuals normalized w.r.t. the 1σ uncertainty band. c) Total measurement time for all retarding energies. Figure from [19].

shown in fig. 2.6 a). Displayed errorbars are enlarged by a factor of 50 for better readability. The data is well described by the model covered in section 2.3.2. The residuals shown in fig. 2.6 b) indicate a very good fit and highlight the dominance of statistical uncertainties. The model consists of four free parameters: The neutrino mass squared m_ν^2, the background rate B, the endpoint E_0 and an additional amplitude similar to C in eq. (2.9). Systematic uncertainties are propagated using MC propagation or a covariance matrix approach. An overview of the systematic uncertainties is given in fig. 2.7. For KNM1 the non-Poisson (NP) background was an important systematic uncertainty. Details of the background model and the implications are discussed in chapter 3. Finally a best-fit value of the neutrino mass squared can be given as in eq. (2.15). Using the methods of Lokhov and Tkachov an upper limit on the neutrino mass is obtained in eq. (2.16), which is the central result of KNM1 and has improved the limits of KATRIN's predecessors by a factor of 2 [19].

$$m_\nu^2 = (-1.0^{+0.9}_{-1.1})\,\mathrm{eV}^2 \tag{2.15}$$

$$m_\nu \leq 1.1\,\mathrm{eV}\,(90\,\%\,\mathrm{C.L.}) \tag{2.16}$$

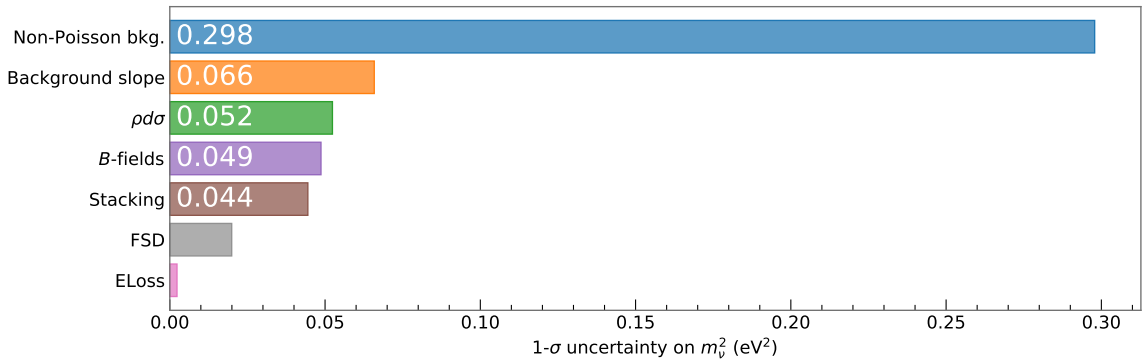

Figure 2.7: Systematic uncertainties for KNM1. Plot by Christian Karl.

Chapter 3

Background

Generally speaking all electrons created in the flux tube of the MS can contribute to the overall background. Electrons from the PS are blocked by the retarding potential which is higher in the MS compared to the PS. The overall background is mainly Rydberg induced as explained in section 3.1. Additionally two contributions arise from radon decays in the main spectrometer and intrinsic detector background [20]. These are presented in section 3.2 and section 3.3 respectively. Other minor sources of background processes are discussed in [20]. This chapter is concluded with a simple way to characterize the background.

3.1 Rydberg-induced background

The main source of background is coming from low-energy electrons being created in the MS. This is sketched in fig. 3.1. As the inner wire electrodes (see section 2.5.4) prevent charged particles from entering the flux tube volume, only neutral atoms can do so. If those atoms are subsequently ionized, this can be a source of background [20].
The underlying processes are radioactive decays occurring in the walls. Those decays can lead to sputtering of neutral atoms, which eventually enter the flux tube volume. Being ionized by thermal radiation, this can lead to low-energy electrons being created. This requires the neutral atom being in a highly exited state (Rydberg state), as the energy of black-body radiation in the MS, which is at room temperature, is otherwise not sufficient. This typically leads to electrons having energies below 100 meV [20].
Low-energetic electrons are guided along the magnetic field lines and accelerated by the retarding potential. This makes them indistinguishable from electrons originating from tritium β-decay. Furthermore this background mechanism scales with the volume between the analysing plane and the detector, hence decreasing this volume could lead to a reduction of this background [20].

3.2 Radon-induced background

While providing high energy resolution and luminosity, one drawback of the MAC-E filter is its equivalence to a magnetic bottle. As on both ends of the MS (see fig. 2.2) the magnetic field is large, charged particles can be trapped. Electrons created in the flux tube are guided by the magnetic field on the one hand, and accelerated by the retarding potential on the other hand. On their way to one of the regions with high magnetic field their longitudinal energy is transferred into transversal energy, as indicated in the bottom of fig. 2.2. If the complete longitudinal energy is transferred, the electron is reflected. This leads to a storage of electrons

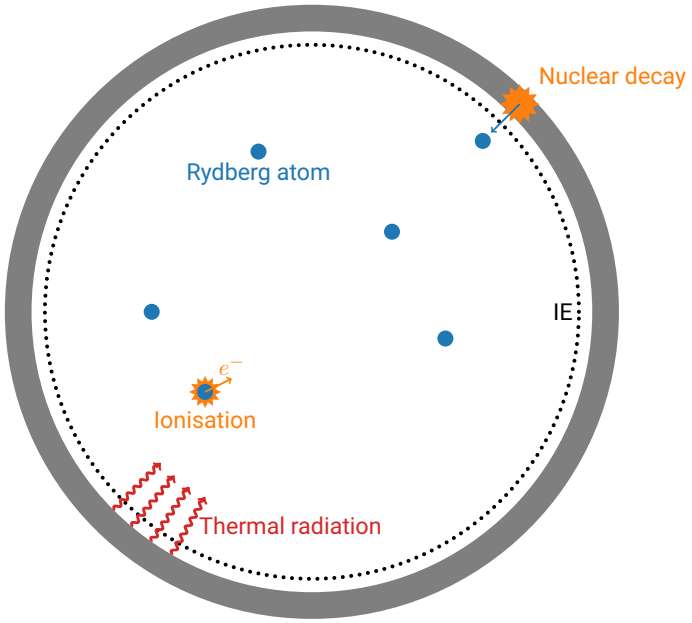

Figure 3.1: Simplified cross section of the main spectrometer. Nuclear decays in its wall can lead to sputtering of highly excited, neutral atoms (Rydberg atoms). Charged particles are blocked by the inner electrode (IE). Rydberg atoms can subsequently be ionised by thermal radiation, creating low energetic electrons [20].

created at position x if eq. (3.1) is fulfilled [20].

$$E_\perp > U_{\text{ret}}(x) \cdot \frac{B(x)}{B_{\text{max}}} \tag{3.1}$$

Therefore electrons with transversal energy larger than the energy resolution of the spectrometer are stored. The motion of a stored electron, as shown in fig. 3.2, consists of axial, cyclotron and magnetron motion. As the radius of cyclotron motion increases linearly with transversal velocity, electrons with higher energy ($\mathcal{O}(100\,\text{keV})$ for usual magnetic field settings) have radii larger than the spectrometer radius. These electrons hence collide with the walls and are not stored [20].
Trapped electrons however follow the motion given in fig. 3.2 until breaking the storage condition. The storage time of such an electron depends mainly on the pressure: Due to scattering with residual gas, it loses energy and changes its momentum, thus eq. (3.1) eventually is not fulfilled anymore and the electron leaves the spectrometer either towards the detector or the source. Secondary electrons created by scattering processes usually leave the spectrometer immediately, being a contribution to the background. As these scattering processes are correlated to some extent, the events are not Poisson distributed [20]. This deviation is a large systematic uncertainty and played an important role in the first neutrino mass measurement [19].
Since the storage condition eq. (3.1) requires a certain amount of (transversal) energy, trapped electrons arise mainly from radon decays. As the MS is continuously pumped out, only radon isotopes with short half-life decay in the flux tube volume. These decays happen homogeneously distributed in the spectrometer. The radon atoms mainly come from the wall where they accumulated before assembly due to natural radioactivity. Furthermore non-evaporable getter (NEG) strips being intended to remove potential residual tritium emanate radon. ^{219}Ra for instance decays in an α-decay. Subsequently electrons are emitted having energies in the range of $1 \times 10^{-3}\,\text{keV}$ to $1 \times 10^{2}\,\text{keV}$. A detailed discussion of the various processes is given in [20].

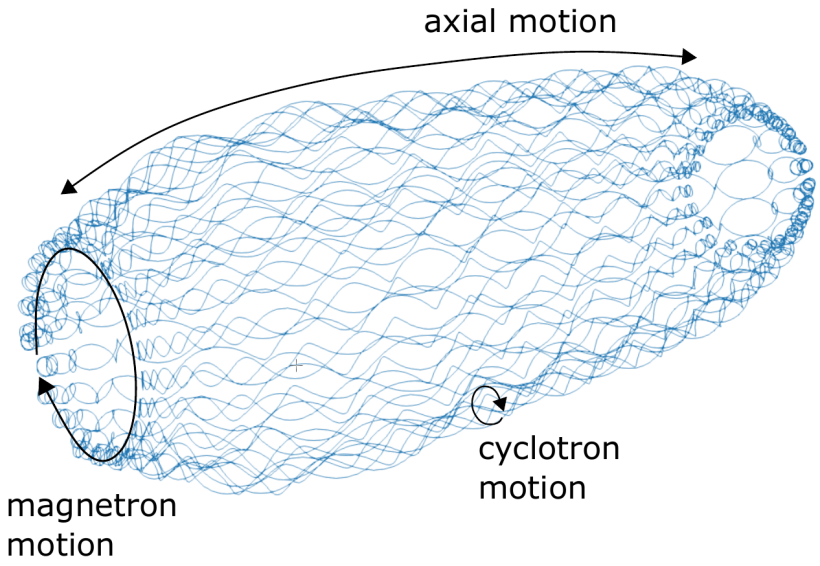

Figure 3.2: Motion of an electron trapped in the spectrometer. It is composed of axial and cyclotron motion along and around the magnetic field lines respectively. Additionally field inhomogeneities lead to magnetron motion [20].

Each emitted electron that is stored in the spectrometer undergoes scattering with residual gas. This leads to multiple secondary electrons, depending on the energy of the primarily stored particle as given in eq. (3.2) [20].

$$N_{\text{secondary}} \approx \frac{E_{\text{primary}}}{\langle E_{\text{loss}} \rangle} \tag{3.2}$$

$\langle E_{\text{loss}} \rangle$ denotes the average energy loss for ionisation while E_{primary} is the energy of the primarily stored electron. For primary electrons with energies of $\mathcal{O}$(keV) this can lead up to $\mathcal{O}(100)$ secondary electrons [20].

3.3 Detector background

The detector background is defined to be present even if there is no connection to the MS. It mainly consists of events following radioactive contaminations of the materials or cosmic rays. To minimise this background, the post-acceleration electrode is used in order to shift the signal to regions of lower intrinsic background. Using a muon scintillator can in principal further reduce this background, but as it is small compared to the Rydberg component this is currently not implemented in the analysis [13, 20].

3.4 Background characterisation

Disentangling the different background components described in the previous sections is a tedious task. The scope of this work however is concentrated on the distinction between Poisson and non-Poisson (NP) background. To this end two simple variables are defined to quantify the deviation of the background distribution from a Poisson distribution (see appendix B.1). Either a relative approach (eq. (3.3)) or an absolute one (eq. (3.4)) is used, depending on ensuing calculations or interpretations. The underlying idea is that time-correlated background leads to a broader distribution of the binned background, as sketched in fig. 3.3. Hence the

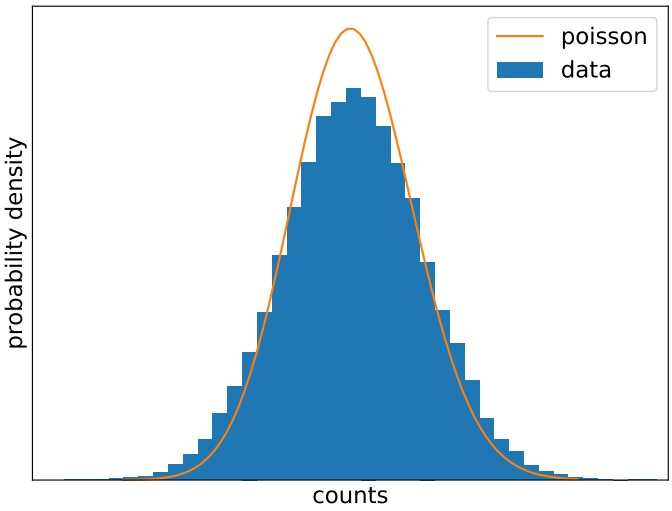

Figure 3.3: Broadening of time-binned background distribution.

measured standard deviation σ is larger than the expected one given by the square root of the mean λ.

$$f_{\mathrm{NP}} = \frac{\sigma}{\sqrt{\lambda}} - 1 \tag{3.3}$$

$$\sigma_{\mathrm{NP}} = \sqrt{\sigma^2 - \lambda} \tag{3.4}$$

While f_{NP} has no unit, σ_{NP} reflects counts hence dividing it by the time t_{bin} used for binning one obtains a quantity usually given in counts per second (cps).
Both f_{NP} and σ_{NP} are zero for no NP component and related via eq. (3.5) with the total background rate $r = \lambda / t_{\mathrm{bin}}$.

$$\frac{\sigma_{\mathrm{NP}}}{t_{\mathrm{bin}}} = \sqrt{\frac{r}{t_{\mathrm{bin}}}} \sqrt{(f_{\mathrm{NP}} + 1)^2 - 1} \tag{3.5}$$

Chapter 4

Monte Carlo background simulation

So as to get a good understanding of the background and in particular its NP component, simulations based on data are performed. In this chapter, a description of the implemented simulation will be given in section section 4.1, followed by its experimental input in section 4.2. Results are presented in section 4.3, effects on the neutrino mass sensitivity are discussed in section 4.4.

4.1 General concept

The MC simulation aims at reproducing the NP characteristic. To this end the total background is divided in two components, one being Poisson distributed and the other representing nuclear decays thus not being Poisson distributed. As for the latter the emitted electrons are stored, additional information about their storage time and the number of secondary electrons they create is needed. Summarizing this, the MC simulation takes the following inputs:

- Poisson rate
- rate of nuclear decays
- storage times
- numbers of secondary electrons

In order to simulate the background and in particular its NP component, the simulation is time-based. After specifying a total time and the step size of individual time bins, the following procedure is repeated for each time step as sketched in fig. 4.1:

1. Draw a random number from a Poisson distribution. The expectation value is calculated from the Poisson rate and the size of the time bin.
2. Similar to step 1 draw another random number based on the rate of nuclear decays. As the nuclear decays itself are independent, they follow a Poisson distribution. For each nuclear decay in this time step, repeat the following sub steps:
   (a) Choose a storage time and the corresponding number of secondary electrons randomly. Calculate the rate of the secondary electrons for this particular nuclear decay, being represented as a cluster. The storage time is hence interpreted as the time for all secondary electrons to hit the detector.

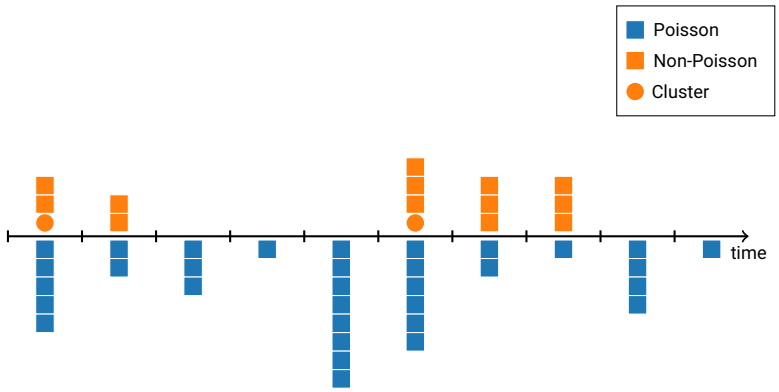

Figure 4.1: Working principle of the MC simulation. In each time bin events coming from a Poisson process are drawn. Subsequently, following experimental inputs, clusters representing nuclear decays are drawn and their induced events are distributed. The starting time of one cluster is indicated as a circle. In principal also more than one nuclear decay can occur in one time step.

(b) Using the previously calculated rate of secondary electrons, estimate which subsequent time steps are affected and how many electrons per step are expected. In each step draw a random number from a Poisson distribution, its mean reflecting the expected number of electrons from the cluster in this time step.

(c) If the affected time steps exceed the total time, ignore all electrons until the last affected bin in the MC range.

This simulation hence gives one large array containing time-resolved information about the electrons being produced. Therefore it offers the possibility to make a connection between the nuclear decay rate and measures of the NP background introduced in section 3.4. Moreover it also allows the simulation of scans providing the opportunity of optimising the measurement strategy of KATRIN, as will be described in section 4.3.3.

4.2 Experimental input

The simulation has to be provided with information about the storage time of a trapped electron together with the number of secondary electrons it creates when scattering with residual gas. This can either be done with another simulation or in a data-driven way. In this work background measurements have been used. So as to allow for an event based distinction of background due to nuclear decays and such coming from Rydberg or the detector, the pressure in the MS has been elevated w.r.t. the pressure in usual tritium operation of 1×10^{-11} mbar. In this way the storage time is reduced, as stored electrons scatter multiple times in a short interval, creating secondary electrons and thus breaking the storage condition (see eq. (3.1)). These decays would manifest themself in a short elevation of the background rate. Furthermore this NP component is visible in the interarrival times. For a pure Poisson distribution these times between two events would follow an exponential distribution. Due to the NP contribution, a deviation from this probability law is expected for short interarrival times.
For this purpose, the pressure in the spectrometers was increased via the injection of argon to 3.0×10^{-9} mbar [21]. Subsequently a 48 h background measurement with a closed valve between the PS and the CPS was performed. Noisy pixels (for KNM1 given in table D.1) are excluded. This dataset will be labelled as background dataset 1 (BKG1) for future reference.

As the rate during this measurement shows no drifts (see fig. 4.2a), the data can be used for ensuing analysis. The interarrival times are shown in fig. 4.2b. The expected deviation from a exponential distribution is visible for small interarrival times. This motivates the definition of a limit $t_{\mathrm{NP}} = 0.3\,\mathrm{s}$ indicating the existence of a NP background component. Therefore interarrival times less than t_{NP} are excluded from the exponential fit in fig. 4.2b.

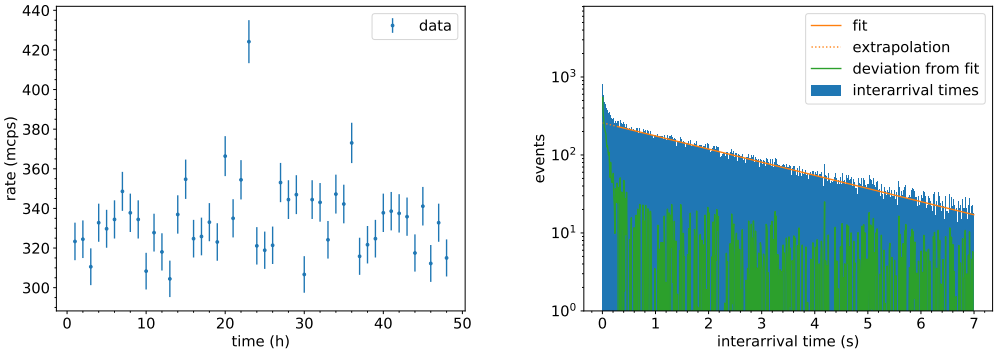

(a) Background rate over time.

(b) Interarrival times

Figure 4.2: (a) Background rate over time of BKG1 using a 1 h time binning. The errors shown are from a Poisson expectation. (b) Interarrival times of BKG1. A deviation from the exponential fit can be seen at short interarrival times. Interarrival times larger than 7 s are neglected.

Furthermore a simple clustering can be applied. Events with an interarrial time less than t_{NP} are grouped in one cluster, as sketched in fig. 4.3. After this clustering, the events in one cluster (its multiplicity) represent the number of secondary electrons of a nuclear decay. The time between the first and the last event (the cluster duration) thus gives an estimate of the storage time of the primary electron. As from a Poisson distribution alone interarrival times less than t_{NP} are expected, one can suppress this random coincidence by only taking clusters with at least 3 events as an input for the simulation. Applying the clustering to the data shown in fig. 4.2b leads to a distribution as shown in fig. 4.4. Most of the clusters have a rather small multiplicity i.e. less than 10 events. The storage time is on the order of a few seconds.

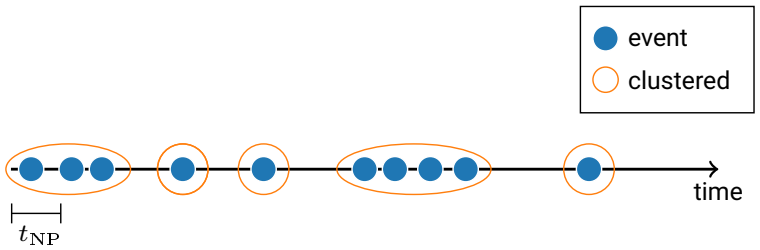

Figure 4.3: Sketch of the clustering. Events with a time difference less than t_{NP} form clusters. Applying cuts on the multiplicity of those clusters suppresses random coincidence.

As the data has been taken at an elevated pressure of $p_0 = 3 \times 10^{-9}\,\mathrm{mbar}$ but the simulation should be performed at usual conditions with a low pressure $p = 1 \times 10^{-11}\,\mathrm{mbar}$, a simple scaling is applied:

$$t = t_0 \cdot \frac{p_0}{p} \tag{4.1}$$

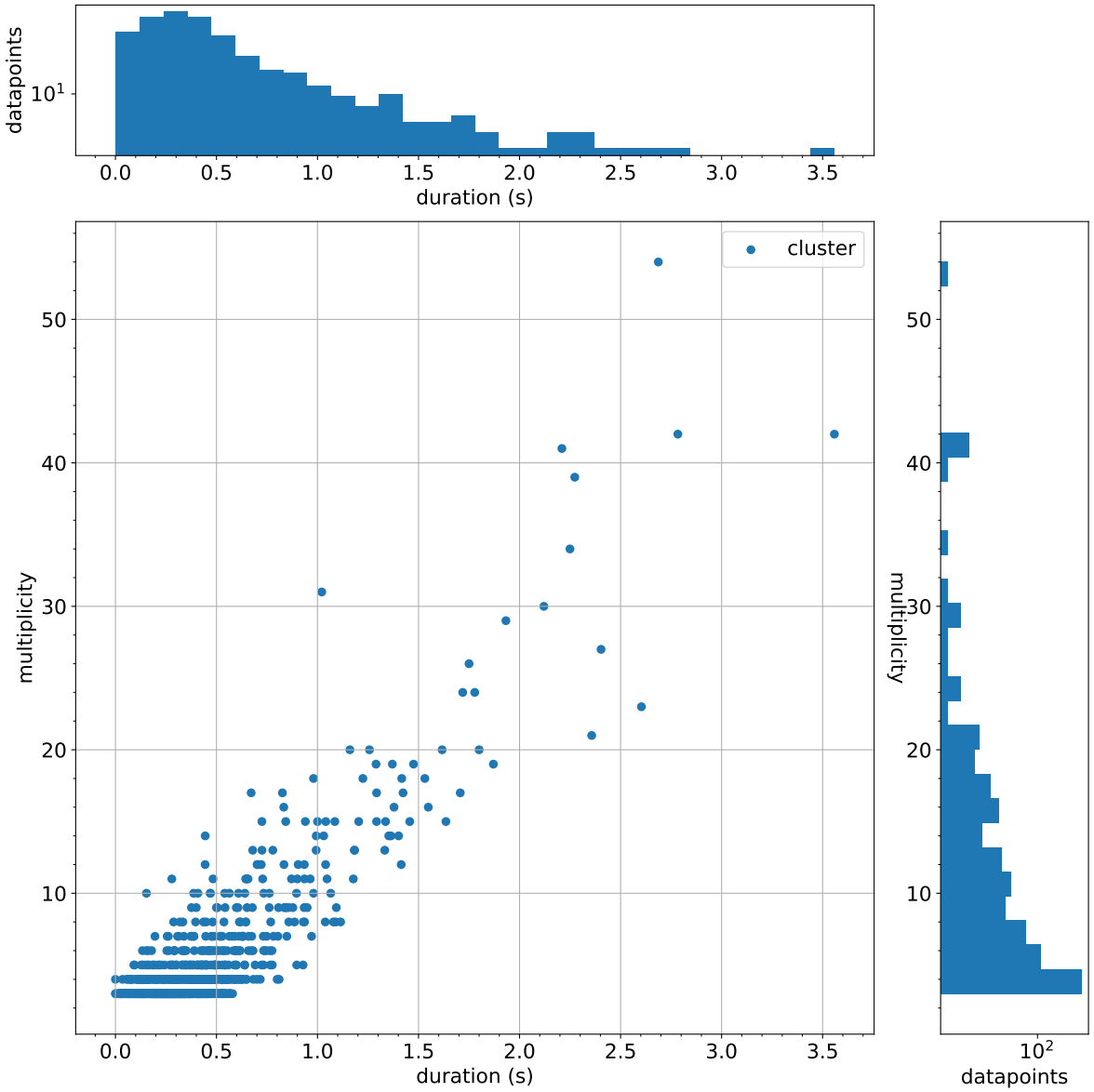

Figure 4.4: Scatter plot of clustered events for BKG1. Clusters containing less than three events are not shown.

p is the pressure at which the simulation is performed, while p_0 refers to the measurement used for the cluster input. For each cluster, the duration t_0 is scaled to t before its taken as an input for the MC simulation. This hyperbolic behaviour is illustrated in fig. 4.5, together with the reference pressure p_o and the mean cluster duration at 1×10^{-11} mbar.

4.3 Results of Monte Carlo simulation

As the simulation of the background is time-based, it offers various possibilities to study the NP background. In this section a brief proof-of-concept will be given, followed by the dependence of f_{NP} on the underlying nuclear decay rate. Moreover effects of the scanning strategy will be analysed, including the effect of scanning the spectrum faster or randomly.

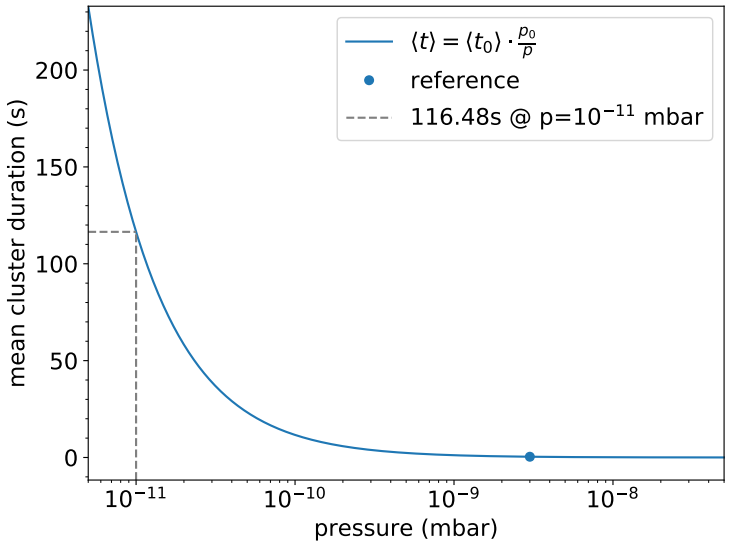

Figure 4.5: Pressure dependence of storage time for BKG1. The reference pressure p_0 and the mean cluster duration at 1×10^{-11} mbar are also shown.

4.3.1 General performance

The simulation aims at reproducing the NP character of the background in an event- and time-based way. As a sanity check the time evolution of the rate can be analysed. To this end the total background rate has been fixed to $r_{\text{tot}} = 200\,\text{mcps}$. Since the simulation requires a Poisson rate together with a nuclear decay rate, r_{tot} is decomposed in two components as given in eq. (4.2). r_{Pois} and r_{NP} reflect electrons induced by Poisson processes and nuclear decays respectively. Subsequently r_{NP} is scaled: On average each nuclear decay leads to $\langle N_{\text{cluster}} \rangle$ electrons hitting the detector. Therefore the rate of nuclear decays needed to achieve r_{NP} is given by r_{cluster} as stated in eq. (4.3).

$$r_{\text{tot}} = r_{\text{Pois}} + r_{\text{NP}} \tag{4.2}$$

$$r_{\text{cluster}} = \frac{r_{\text{NP}}}{\langle N_{\text{cluster}} \rangle} \tag{4.3}$$

In this example the NP ratio was chosen to be $r_{\text{NP}}/r_{\text{tot}} = 11\,\%$. Information about the clusters were taken from fig. 4.4 using only clusters with at least three events to suppress random coincidence. A continuous background measurement at 1×10^{-11} mbar lasting 60 d has been simulated.
Figure 4.6 shows the time evolution of the rate using a 1 h binning. The rate is calculated separately for Poisson and NP induced events. For simplicity the errors are not shown directly but the rate projection is displayed. The first sanity check is the consensus between the calculated and expected width of the simulated Poisson background. As the NP induced events are shown separately the clear disagreement of the rate projection with a Poisson expectation is visible. The corresponding width is given by 7.8 mcps while it is expected to be 2.5 mcps. This leads to a total background with a width of 10.5 mcps that translates into $f_{\text{NP}} = \frac{10.5}{7.5} - 1 \approx 40\,\% > 0$ as t_{bin} cancels. Thus the NP characteristic could be reproduced successfully. It should be noted that f_{NP} and $r_{\text{NP}}/r_{\text{tot}}$ do not necessarily agree as the former depends on the time binning while the latter does not. This is illustrated in section 4.3.3.

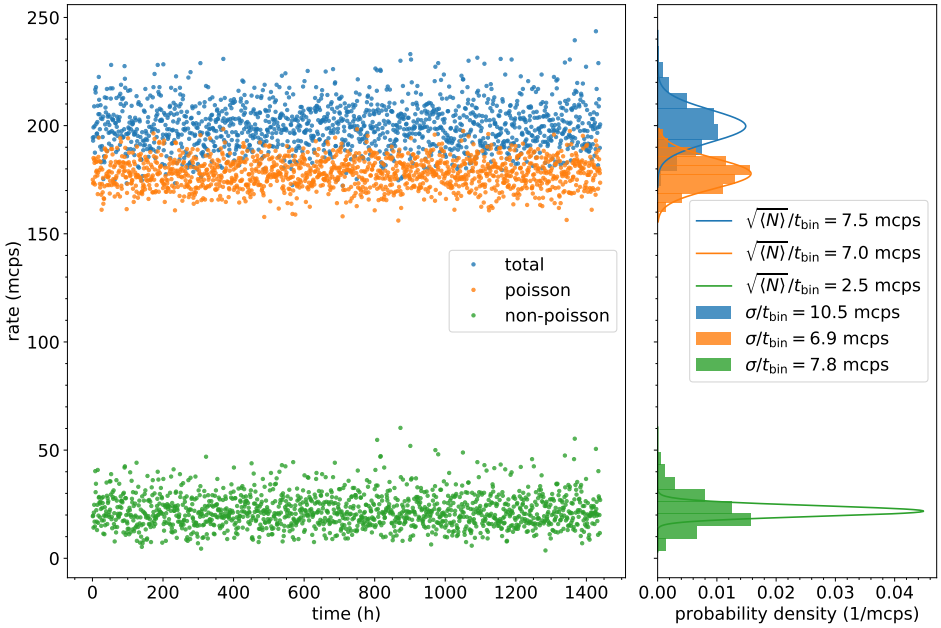

Figure 4.6: Rate over time for MC simulated data. The total rate is fixed to 200 mcps, $r_{\mathrm{NP}}/r_{\mathrm{tot}} = 11\,\%$. The rate projection is shown on the right hand side. Expected and calculated width of the distributions are given in the legend.

4.3.2 f_{NP} dependence on nuclear decays

As the non-Poisson component is induced by nuclear decays in the main spectrometer, the dependence of f_{NP} on the nuclear decay rate is investigated. In this analysis the total background rate has been fixed to $r_{\mathrm{tot}} = 200$ mcps. The cluster input is the same as previously, clusters with less than 3 electrons are ignored. Then multiple MC simulations are performed varying the NP ratio $r_{\mathrm{NP}}/r_{\mathrm{tot}}$ between 0 and 0.10. For each value a 60 d background measurement is simulated. This procedure is repeated for different pressures.
Figure 4.7 shows the result of the simulation. Each points hence represents a 60 d background simulation being binned in 360 s intervals to calculate f_{NP}. The time binning corresponds approximately to the measurement time spent at each background point during a 2 h scan. Uncertainties of f_{NP} are estimated via bootstrapping[1]. A simple linear function is fitted for each pressure to underline the linear trend of f_{NP} with $r_{\mathrm{NP}}/r_{\mathrm{tot}}$. An estimate of f_{NP} during the second neutrino mass measurement phase is shown in grey as a reference.
While the slope difference between 1×10^{-11} mbar and 1×10^{-10} mbar is well pronounced, the step from 1×10^{-10} mbar to 1×10^{-9} mbar is barely visible. As explained in section 4.2 the cluster duration is scaled inversely with the pressure. Hence for lower pressure one primary electron is stored for a longer amount of time as there is less residual gas. This behaviour is depicted in fig. 4.5. Following this scaling the expected difference of the mean cluster duration between 1×10^{-10} mbar and 1×10^{-9} mbar is rather small. However going to 1×10^{-11} mbar increases the cluster duration significantly thus a larger gap is expected. This is clearly reflected in fig. 4.7. This implies that an increase of the storage time is beneficial for a reduction of the NP fraction. If they primary electron is stored for an extended amount of time, the created secondary electrons spread over multiple time bins and the time-correlation becomes less visible.
Moreover this simulation allows for a translation of a measured NP fraction in terms of f_{NP} into a nuclear decay rate. However for this the cluster distribution has to be known precisely as the simulation mainly depends on this input.

[1] Bootstrapping here means resampling the dataset multiple times to estimate erros, see also [22].

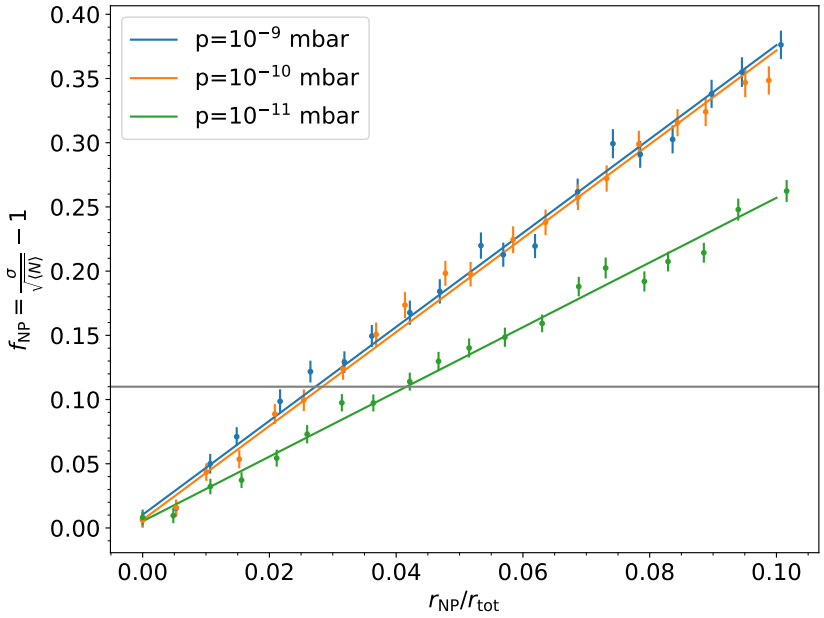

Figure 4.7: Dependence of f_{NP} on the nuclear decay rate for various pressures, with fixed $r_{\mathrm{tot}} = 200\,\mathrm{mcps}$. The grey line indicates an estimation of f_{NP} during the second neutrino mass measurement phase. Errors on f_{NP} are obtained using bootstrapping.

4.3.3 Scanning strategy

KATRIN measures the neutrino mass by scanning the integral tritium spectrum at different retarding potentials as described in section 2.6. The time spent at each potential is optimised such that the sensitivity on the neutrino mass is maximal. This leads to a peak in the measurement time distribution (MTD) close to the endpoint E_0 as shown in fig. 4.8 for $E_0 = 18\,575\,\mathrm{eV}$. Usually these retarding potentials are scanned alternatingly up and down, each scan lasts 2 h. However previous studies have shown that scanning faster or randomly can improve the m_ν sensitivity [23].

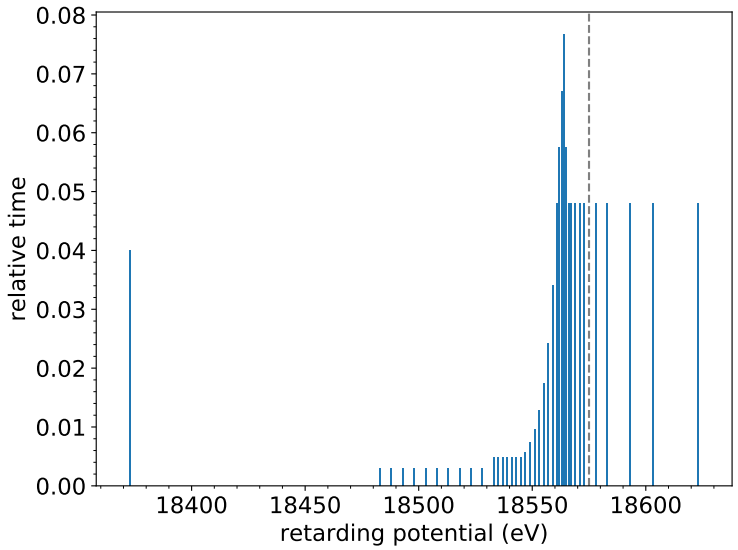

Figure 4.8: Measurement time distribution. The endpoint $E_0 = 18\,575\,\mathrm{eV}$ is indicated in grey.

In this section the effect of the MTD on a NP background is investigated. Firstly the dependence of f_{NP} on the underlying time binning is examined. Analogous to previous studies the total rate is fixed to 200 mcps. In order to simulate a realistic scenario, $r_{\mathrm{NP}}/r_{\mathrm{tot}}$ is chosen so that $f_{\mathrm{NP}} = 11\,\%$ for a time binning of 360 s. This is motivated by the NP fraction during the second neutrino mass campaign as indicated in fig. 4.7 and discussed previously.
Simulating 60 d of background at $p = 1 \times 10^{-11}$ mbar thus allows to calculate f_{NP} for several time binnings. These binnings usually refer to the duration of a subscan in the background region of the MTD above the endpoint. As the measurement times for the background points are equal, they can be stacked when calculating f_{NP} and one subscan time is enough to describe the NP fraction in this region.
Figure 4.9 shows how f_{NP} changes with subscan time. While the NP fraction decreases for short subscans, it settles if the subscan duration is increased. Uncertainties are estimated via bootstrapping and thus increase for longer subscans as the number of subscans is given by the total measurement time divided by the subscan time.
This behaviour of limited growth can be explained by the nature of the NP background. A stored electron produces multiple secondary electrons hitting the detector. If these electrons are spread over multiple subscans due to their short duration, the NP fraction becomes less visible. On the other hand long subscans may contain all secondary electrons from one nuclear decay. Hence for extended subscans f_{NP} settles. As nuclear decays may happen anytime during one subscan its duration needs to be significantly larger than the average storage time of an electron. In this simulation the mean storage time is about 2 min (see fig. 4.5) but the bound is reached at $\mathcal{O}(10\,\mathrm{min})$.
As already displayed in fig. 4.8 the measurement time is increased in the most sensitive region just below the tritium endpoint. Then again it is short deeper into the spectrum (except for the monitoring point) as the rates are higher. Due to the subscan dependence of f_{NP} one value may not be enough to characterise the background for all subscans. Instead one value per subscan seems to be more appropriate. Moreover a nuclear decay occurring in one subscan may still lead to an elevated background rate in adjacent subscans. This would introduce correlations between the subscans as they are no longer completely independent.
Simulating the correlations is done via emulating the MTD when binning the background

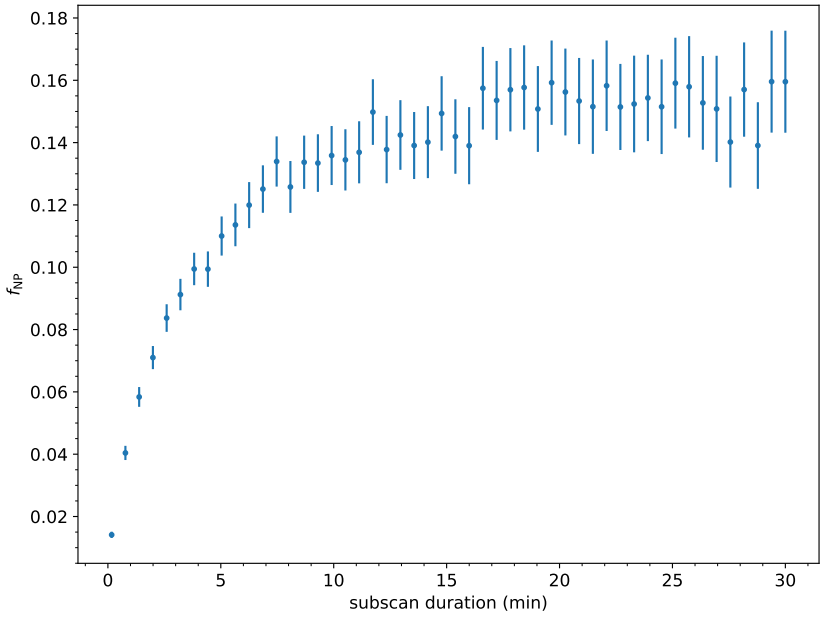

Figure 4.9: Simulated effect of subscan duration NP fraction for $r_{\mathrm{tot}} = 200\,\mathrm{mcps}$ at $p = 1 \times 10^{-11}$ mbar. Uncertainties are estimated using a bootstrap.

data. This allows to calculate f_{NP} individually for each subscan and furthermore to estimate the correlations induced by the elevated background rate. The shown MTD consists of 40 points, which will be labelled from 0 to 39 in ascending order. Whereas the subscan dependence is considerably visible for a realistic background scenario as shown in fig. 4.9 this does not hold for the correlations between subscans. Therefore in the following a scenario with exaggerated NP background will be explored to analyse the consequences before investigating the implications on the neutrino mass in a KATRIN neutrino mass 2 (KNM2) like scenario in section 4.4.

A worst case scenario

To explore the effects of nuclear decays thoroughly, a different experimental input as described in section 4.2 is used. In the maintenance phase of KATRIN an incident lead to residual tritium reaching the main spectrometer. This caused a temporary elevated background and an increased NP contribution. As tritium is continuously pumped out, the background rate was less stable than usual as can be seen in fig. 4.10a (for the pixel selection see KNM2 in table D.1) [24]. As an unstable rate would lead to inconsistent interarrival times, only data after 60 h of the measurement has been used for ensuing calculations and simulations. This dataset is labelled as background dataset 2 (BKG2) in the following.
The corresponding distribution of interarrival times for BKG2 is shown in fig. 4.10b. The deviation from an exponential distribution is much larger compared to fig. 4.2b. Moreover this measurement was performed at 2.8×10^{-8} mbar thus the storage time is further reduced. This motivates to define clusters to have an interarrival time of less than $t_{\mathrm{NP}} = 0.2\,\mathrm{s}$ and group the events accordingly.
Figure 4.11 shows the cluster distribution, revealing higher multiplicities for similar durations. Moreover small clusters dominate. This is mostly due to residual tritium molecules decaying in the spectrometer. In the following, these clusters are used as an input for the MC simulation.

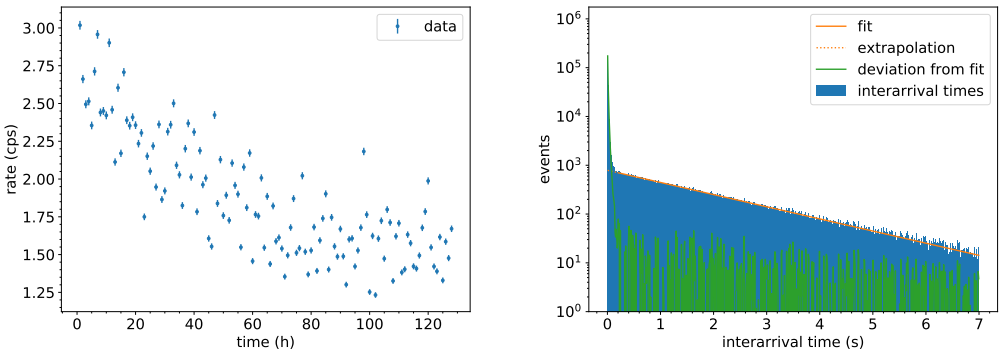

(a) (b)

Figure 4.10: (a) Background rate over time after the tritium incident using a 1 h time binning. The errors shown are from a Poisson expectation. (b) Interarrival times of BKG2 (i.e. only events after 60 h w.r.t. (a) are considered). A deviation from the exponential fit can be seen at short interarrival times. Interarrival times larger than 7 s are neglected.

Given the data for the nuclear decays, i.e. storage time and number of secondary electrons from fig. 4.11, multiple MC samples were generated. Each MC sample represents 60 d of background with a total rate of 200 mcps. The pressure is set to be 1×10^{-11} mbar, while the

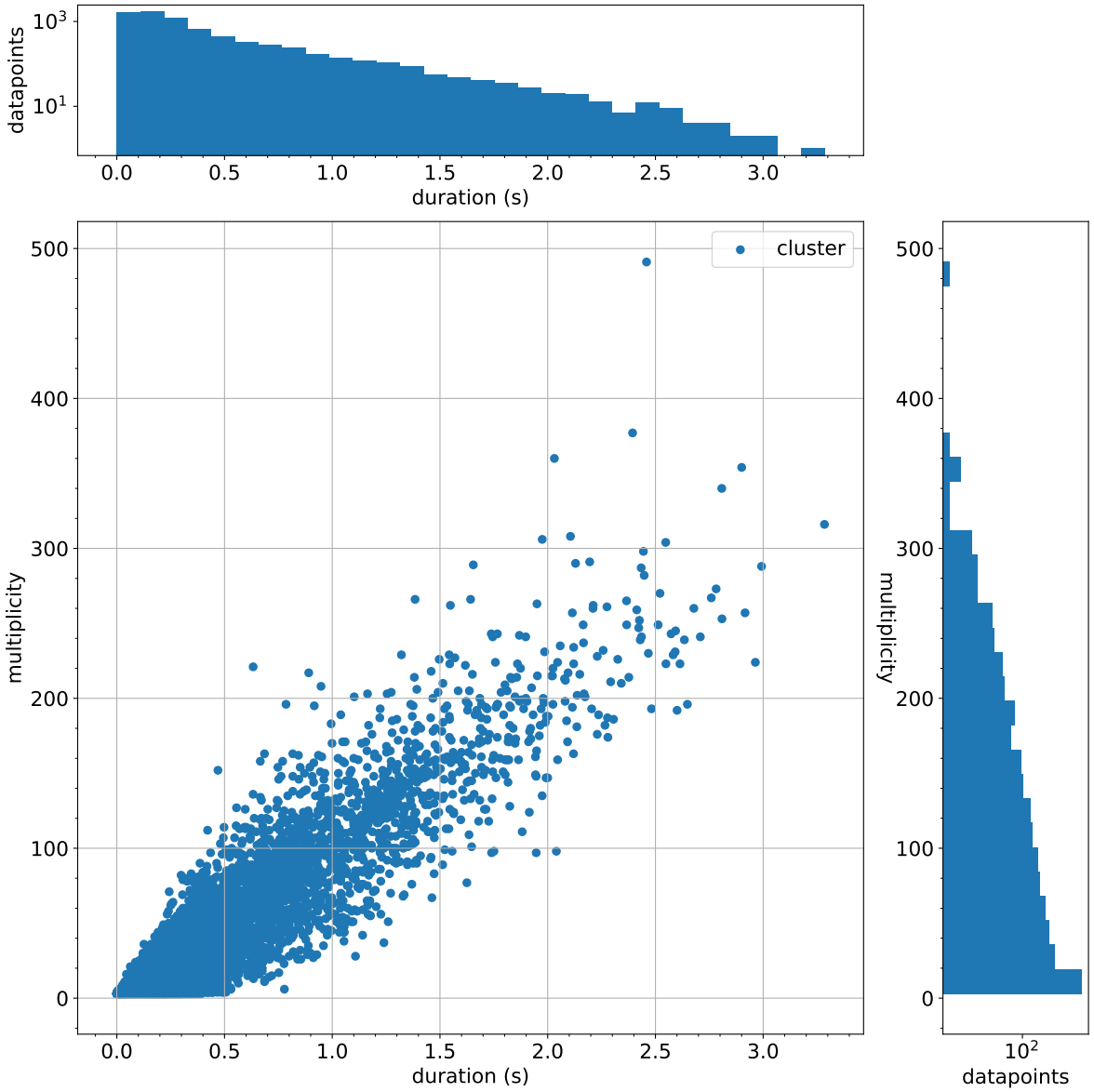

Figure 4.11: Scatter plot of clustered events of BKG2. Clusters containing less than three events are not shown.

rate of nuclear decays was fixed such that $r_{\mathrm{NP}}/r_{\mathrm{tot}} = 11\,\%$[2].
The time-resolved background can then be binned using the MTD. This is done emulating alternating up and down scans as well as random scans. Besides that the scantime can be varied.
Figure 4.12a shows the NP induced correlations between different subscans. As a reference the MTD is depicted in fig. 4.12b again. While the correlations are confined along the diagonal close to the endpoint they are more evenly spread for subscans deeper into the spectrum. This reflects the measurement time distribution accordingly. Secondary electrons can either spread over multiple short subscans or be concentrated in a few long subscans. As the NP background only increases the rate, negative correlations are not expected.
Scanning faster is depicted in fig. 4.13a for the usual up/down scanning procedure. Compared to fig. 4.12a the correlations are more smeared and less confined to the diagonal. As the scantime decreases, the amount of affected subscans per nuclear decay increases.

[2]This was shown to be exaggerated previously thus it fits very well for this worst case scenario.

The spread of the correlations is even more pronounced when the retarding potentials are scanned randomly as displayed in fig. 4.13b. Since the order of subscans may be different in each scan correlations eventually average out to some extent.
If the scantime is shorter, the correlations are more evenly distributed on all subruns. This can even by enhanced when the spectrum is scanned randomly. In order to evaluate these effects and their implications on the neutrino mass sensitivity, correlations and subscan dependent NP fractions are included in the analysis as discussed in the following section.

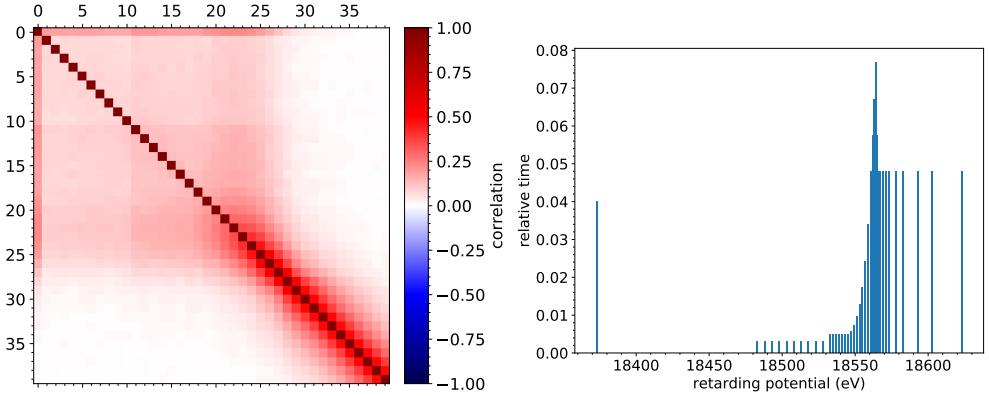

(a) (b)

Figure 4.12: (a) Correlations for up/down scanning with 2 h scantime. (b) Measurement time distribution.

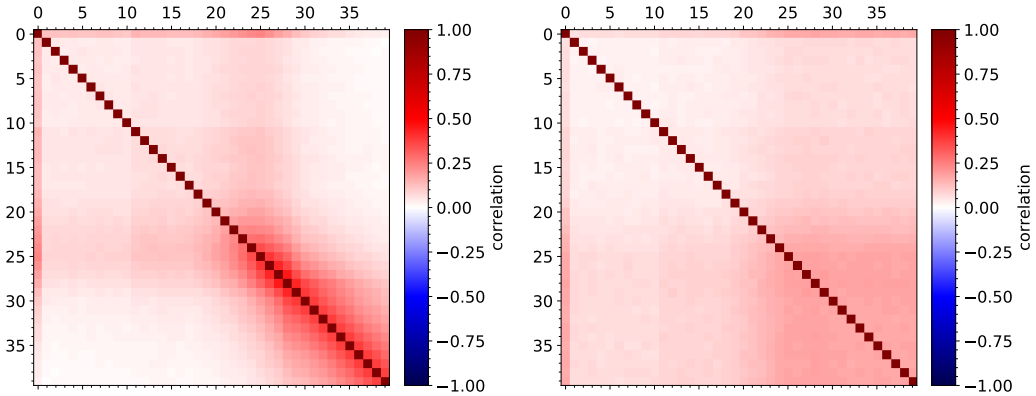

(a) up/down scanning (b) random scanning

Figure 4.13: (a) Correlations for up/down scanning with 1 h scantime. (b) Correlations for random scanning with 2 h scantime.

4.4 Effects on the neutrino mass sensitivity

The NP background introduces correlations between subscans that can be reduced by scanning faster or randomly. Moreover f_{NP} depends on the duration of one subscan and decreases for shorter durations as events spread over multiple subscans. In the usual analysis the NP fraction is quantified using a single value only. However it may be more appropriate to use a subscan dependent f_{NP} since the measurement time distribution is not uniform. In order to evaluate these different treatments and countermeasures the neutrino mass sensitivity has to be calculated for each of them.

Including systematic uncertainties can be done using covariance matrices as described in section 2.4. In this case the total covariance matrix is calculated via eq. (4.4). In addition to statistical uncertainties represented by V_{stat} the NP background is included via V_{NP}. It is defined using eq. (4.5) where i denotes the label of the corresponding subscan. Correlations can be taken into account using $C^{(i,j)}$ and neglected by setting $C^{(i,j)} = \delta_{i,j}$[3]. The NP background leads to a relatively larger uncertainty on the rate. However similar to the statistical uncertainty it decreases with measurement time hence V_{NP} is divided by the number of scans as given in eq. (4.6).

$$V_{\text{tot}} = V_{\text{stat}} + V_{\text{NP}} \tag{4.4}$$

$$\tilde{V}_{\text{NP}}^{(i,j)} = C^{(i,j)} \cdot \frac{\sigma_{\text{NP}}^{(i)}}{t^{(i)}} \cdot \frac{\sigma_{\text{NP}}^{(j)}}{t^{(j)}} \tag{4.5}$$

$$V_{\text{NP}}^{(i,j)} = \frac{\tilde{V}^{(i,j)}}{N_{\text{scans}}} \tag{4.6}$$

A short sanity check of eq. (4.6) is given in the following: Considering a general process with a constant rate of events r, this rate can be obtained by measuring for a finite amount of time t and count the number of events N. A simple division as in eq. (4.7) gives an estimate on the rate of events. For a Poisson process, the uncertainty can be calculated using eq. (4.8).

$$r = \frac{N}{t} \tag{4.7}$$

$$\sigma_r = \frac{\sqrt{N}}{t} \tag{4.8}$$

Substituting eq. (4.7) into eq. (4.8) thus gives

$$\sigma_r = \sqrt{\frac{r}{t}} \sim \frac{1}{\sqrt{t}} \tag{4.9}$$

which decreases over time. An additional NP component increases the uncertainty σ_r in a relative way. This relative contribution is not expected to be measurement time dependent for a constant nuclear decay rate. Therefore V_{NP} should decrease over time similar to a statistical uncertainty. Inserting $N_{\text{scans}} = t_{\text{measured}}/t_{\text{scan}}$ in eq. (4.6) using the relation given in eq. (3.5) subsequently yields

$$V_{\text{NP}}^{(i,i)} = \frac{\tilde{V}^{(i,i)}}{N_{\text{scans}}} \sim \left(\frac{\sigma_{\text{NP}}^{(i)}}{t^{(i)}}\right)^2 \cdot \frac{t_{\text{scan}}}{t_{\text{measured}}} \tag{4.10}$$

$$\sim \left(\sqrt{\frac{r}{t^{(i)}}}\sqrt{(f_{\text{NP}}^{(i)}+1)^2 - 1}\right)^2 \cdot \frac{t_{\text{scan}}}{t_{\text{measured}}} \tag{4.11}$$

$$\sim r\left((f_{\text{NP}}^{(i)}+1)^2 - 1\right) \cdot \frac{1}{t_{\text{measured}}} \tag{4.12}$$

where in the last step the relation $t_{\text{scan}} \sim t^{(i)}$ was used which is implied by the MTD.
This matrix can now be calculated for different background scenarios and scanning strategies. In the final step the full covariance matrix is used to fit a MC spectrum generated beforehand using Fitrium (an overview of the parameters used for generation is given in appendix C, for simplicity only one pixel is considered for generating and fitting MC spectra). As in addition to a KNM2 like background scenario a hypothetical situation of a dominant NP background has been investigated, the sensitivity defined by eq. (4.13) will be evaluated for both cases. $\sigma^+(m_\nu^2)$ represents the upper asymmetric error of m_ν^2.

$$m_\nu < \sqrt{1.645 \cdot \sigma^+(m_\nu^2)}\ (90\,\%\ \text{C.L.}) \tag{4.13}$$

[3] $\delta_{i,j}$ represents a Kronecker delta, i.e. it is 1 if $i = j$ and 0 otherwise.

4.4.1 The worst case scenario

Estimating the effectiveness of random scanning w.r.t. the reduction of the correlations is done by comparing it to usual up/down scanning. Moreover this is done for different scantimes. The results assuming the worst case background model from section 4.3.3 are displayed in fig. 4.14. As a reference the sensitivity for up/down scanning neglecting correlations is given. The statistical uncertainty (no NP background contribution) is shown as well (dashed).
In each case faster scanning improves the m_ν sensitivity. Moreover random scanning reduces the correlations and is similar to a (hypothetical) case of no correlations.

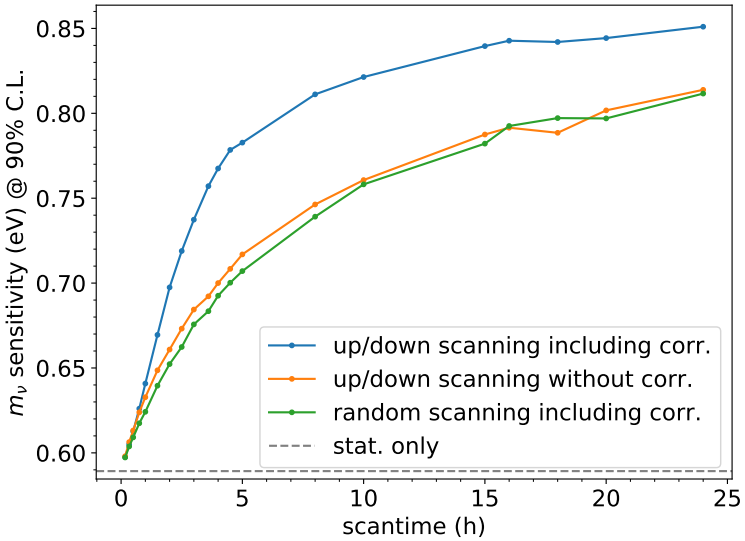

Figure 4.14: m_ν sensitivity for different scanning strategies after 60 d of consecutive data taking. The underlying background model assumes an exaggerated NP background with $r_{\mathrm{tot}} = 200\,\mathrm{mcps}$ and $r_{\mathrm{NP}}/r_{\mathrm{tot}} = 11\,\%$.

4.4.2 A KNM2 like scenario

In order to estimate possible improvements for a KNM2 like scenario (30 d measurement time), two realistic background models are used. The cluster input consists of BKG1 as discussed beforehand.
The input parameters of the models are given in table 4.1, differing in the total rate and the NP component. The ratio $r_{\mathrm{NP}}/r_{\mathrm{tot}}$ is chosen according to fig. 4.7 such that f_{NP} calculated at the usual time spent at each background point of $t_{\mathrm{bin}} = 360\,\mathrm{s}$ yields the intended value of 11 % or 5 % respectively. To this end, a similar estimation as in fig. 4.7 is performed for a fixed rate of 100 mcps.

Table 4.1: MC background models

model	r_{tot} in mcps	f_{NP} in %	$r_{\mathrm{NP}}/r_{\mathrm{tot}}$
200 mcps	200	11	0.043
100 mcps	100	5	0.019

For the models specified in table 4.1 100 MC simulations are performed each. Similarly to the

worst case scenario, covariance matrices are computed and then used for fitting an Asimov spectrum.
Figure 4.15 shows a similar effect as in the worst case scenario (correlations are included). However, the improvement by scanning faster is smaller as the NP component is less dominant. Furthermore, the difference between up/down and random scanning is less pronounced. In the case of small NP background the improvement using faster or random scanning is hence more limited.

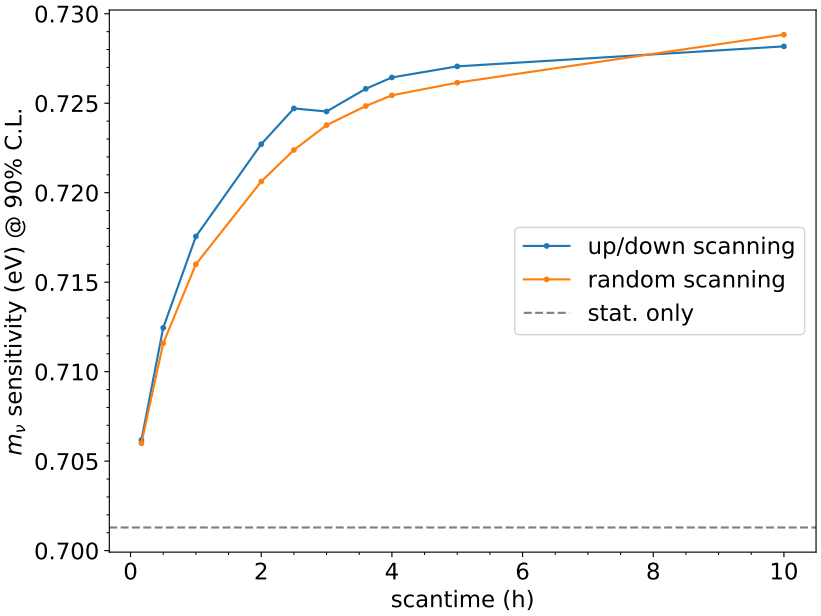

Figure 4.15: m_ν sensitivity for different scanning strategies. The total measurement time is fixed to 30 d, the total background rate is 200 mcps (see table 4.1).

As the usual scantime for KATRIN is 2 h, improvements for this case are most important. Estimating the NP component for real data is only possible for the background points of the MTD. Therefore only one value f_{NP} is known since the measurement time is equal for all background points. The covariance matrix hence can be calculated with this value only. This is implemented in this simulation by setting $C^{(i,j)} = \delta_{i,j}$ and using f_{NP} from the background points above the endpoint exclusively. This allows for a comparison of three different methods to calculate the covariance matrix:

1. One (global) value characterising the NP background. This is assumed to be identical for all subscans. Correlations are neglected.

2. One value per subscan, obtained by setting $C^{(i,j)} = \delta_{i,j}$ in eq. (4.5).

3. One value per subscan including correlations.

The comparison of these three different ways (using alternating up and down scans of 2 h) is shown in fig. 4.16a for the 200 mcps scenario (see table 4.1). The corresponding numerical values are given in table 4.2. The differences between these three methods are less than 2.6 %. For a realistic scenario, correlations or a subscan dependent NP component are hence negligible. It should therefore be sufficient to use one value of f_{NP} to fully characterise the NP nature of the background.
Figure 4.16b shows the scaling of the total uncertainty with measurement time for the two different background scenarios specified in table 4.1. A NP background manifests itself in a shift of the sensitivity. This implies that the effect is in particular large for long measurements

when small changes of the sensitivity require large amounts of additional measurement time.

Table 4.2: Sensitivity on m_ν after 30 d for 200 mcps background.

method	m_ν sensitivity in eV
stat. only	0.701
1	0.721
2	0.721
3	0.723

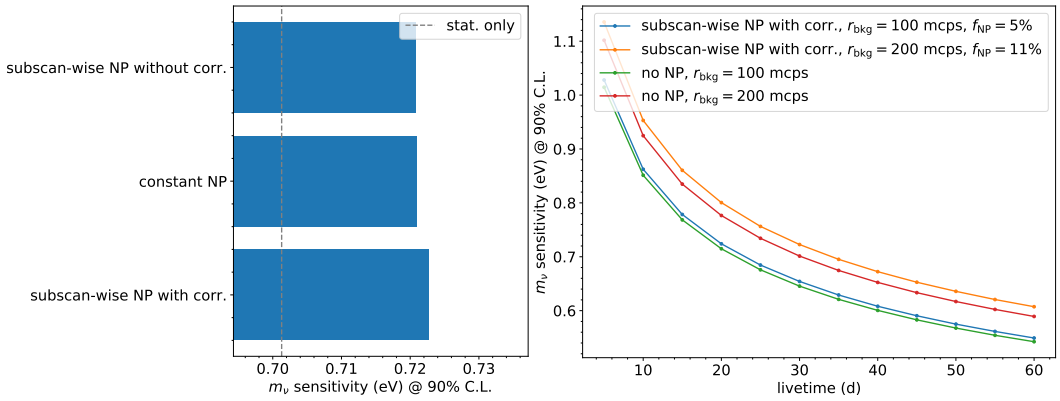

(a) (b)

Figure 4.16: (a) m_ν sensitivity for different approaches to calculate the covariance matrix. The underlying model assumes a background rate of 200 mcps (see table 4.1) and 30 d measurement time. (b) Neutrino mass sensitivity as a function of measurement time for different background situations.

4.4.3 Intermediate conclusion

The results of the MC simulation can be summarised as follows: Using experimental data as input, a time-based simulation of the background can be performed. This reproduces the NP nature as seen in experimental data. Furthermore it offers the possibility to deduce an estimation of the underlying nuclear decay rate. This requires precise knowledge of the cluster distribution.
Scanning faster and randomly can in principal improve the neutrino mass sensitivity as the NP fraction and subscan correlations are reduced respectively. However these effects are very limited for a realistic background scenario. In addition waiting times due to high voltage stabilisation increase for faster and random scanning. This may eventually lead to a deterioration of the neutrino mass sensitivity.
Despite being subscan dependent one value of f_{NP} is enough to fully describe the NP background in a KNM2 like scenario. Moreover correlations can be neglected without any substantial error.
The NP background is similar to a shift of the sensitivity w.r.t. the measurement time. Therefore it becomes important if the statistics increase as an improvement requires a large amount of measurement time.

Chapter 5

Shifted Analysing Plane

In order to reach the design sensitivity of $m_\nu = 0.2\,\mathrm{eV}$ (90 % C.L.), a background of 10 mcps was proposed [13]. However during KNM1 the observed background was (293 ± 1) mcps thus exceeding the design sensitivity by more than one order of magnitude [19]. As described in chapter 3 the majority of the background is coming from Rydberg atoms. Hence reducing this contribution would be most beneficial for the sensitivity. A promising idea is the shifted analysing plane (SAP) explained in section 5.1. Needed calibration measurements using a gaseous krypton source are discussed in section 5.2, the effect on the KATRIN m_ν sensitivity is covered in section 5.3.

5.1 Concept

Electrons created through the Rydberg mechanism have low energies compared to the retarding potential. This makes it effectively impossible for them to overcome the potential barrier situated in the analysing plane (AP). Only electrons created in the volume enclosed by the AP and the FPD can hence contribute to the background. This volume is referred to as downstream volume. During KNM1 it was around $160\,\mathrm{m}^3$ in symmetric settings. Reducing the downstream volume by shifting the AP towards the FPD (depicted in fig. 5.1) therefore simultaneously reduces the Rydberg background. Shifting the AP is achieved by using different electromagnetic settings as in the nominal mode where it is in the center of the spectrometer. Theses changes however introduce inhomogeneities in the electric and magnetic fields in the AP. Furthermore the storage conditions due to non-adiabiatic motions are different. In total a background reduction of about 2 for the Rydberg induced background is expected. Moreover the NP fraction presumably decreases as the storage conditions are worse [20].
Despite decreasing the background the introduced inhomogeneities may harm the sensitivity of KATRIN. Depending on the path the electrons take in the spectrometer, the experienced magnetic field may be different. This leads to a higher uncertainty on these fields that is reflected in a worsened sensitivity on the neutrino mass. To avoid this, dedicated measurements need to be performed to confirm the knowledge of the fields in the AP. Those measurements are described in section 5.2.

5.2 Magnetic field calibration

Measuring the electric and magnetic fields in the AP is a tedious task. It is not possible to obtain them directly, but using electrons from a source with well known energy and angular distribution offers a possibility to extract these fields. In KATRIN this is possible using a

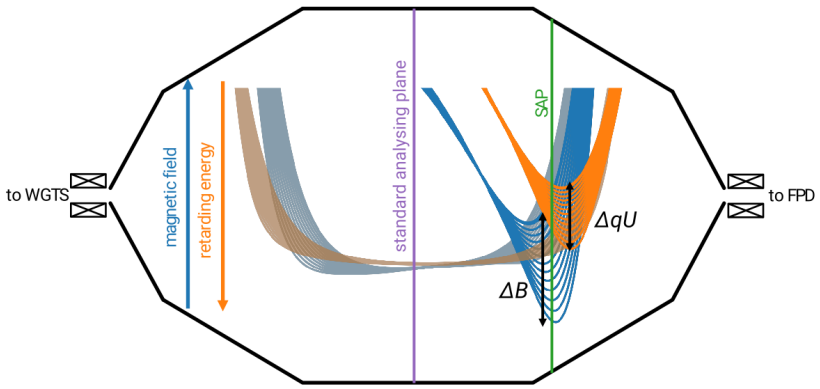

Figure 5.1: Sketch of the shifted analysing plane. The previously centered analysing plane (purple) is shifted (green) towards the detector. This introduces inhomogeneities in the electric and magnetic fields. Solid lines correspond to the SAP setting, transparent lines to the standard analysing plane. Figure adapted from [20].

photo-electronic or a krypton source. This work focuses on the krypton source. Its properties together with the model are briefly described in section 5.2.1. The selection of data and a short pre-evaluation is given in section 5.2.2 while section 5.2.3 focuses on the analysis strategy. The results and the effect on the neutrino mass sensitivity are presented in section 5.2.4.

5.2.1 Krypton source and model

Inserting the metastable isotope $^{83\mathrm{m}}$Kr into the WGTS offers the possibility to conduct various calibration measurements. In its decay, many mono-energetic conversion electrons are emitted. Of particular interest is the conversion line with an energy of 17.8 keV, in the following denoted as K-32 line. As its energy is close to the tritium endpoint, it may serve as a tool for characterising electric and magnetic fields used in tritium operation mode. Its (differential) spectral shape is described using a Lorentzian function as given in eq. (5.1). The width for the K-32 line is about $\Gamma = 2.7\,\mathrm{eV}$. E_0 denotes the centroid value of 17.8 keV, A refers to an amplitude such that eq. (5.2) holds [25].

$$L(E; A, E_0, \Gamma) = \frac{A}{\pi} \frac{\Gamma/2}{(E - E_0)^2 + \Gamma^2/4} \tag{5.1}$$

$$\int_{-\infty}^{+\infty} L(E; A, E_0, \Gamma)\,\mathrm{d}E = A \tag{5.2}$$

Similar to the model of the tritium spectrum, additional modifications are applied. In particular $L(E; A, E_0, \Gamma)$ is corrected for thermal Doppler broadening. To obtain the integral spectrum, it is then convolved with the response function. Since in the case of krypton scattering in the source is negligible, the response function in this case consists only of the transmission function specified in eq. (2.7). The integral spectrum is then given by eq. (5.3). The background is assumed to have a linear slope given by m_{bkg}, see eq. (5.4). As the energy of the K-32 line is below the tritium endpoint, additional background arises from residual tritium in the rear section. Contrary to the contributions discussed in chapter 3 this is expected to be retarding potential dependent. This was confirmed in a short background measurement with an empty source. Figure 5.2a shows a retarding potential dependent rate exemplary for pixel 0. As expected from the shape of the integral tritium spectrum the slope is negative. An exemplary fit of the K-32 line in the SAP setting for one pixel is depicted in fig. 5.2b. The normalised residuals show no apparent structure indicating that the model describes the data well. In particular one background point being further away from the krypton line itself

is fitted precisely with a linear slope. For this fit the χ^2 was 24.2 at 35 degrees of freedom resulting in a p-value of 0.92.

$$S(qU) = \int_{qU}^{+\infty} L(E; A, E_0, \Gamma) \cdot T(qU, E)\,\mathrm{d}E + B(qU) \tag{5.3}$$

$$B(qU) = B_{\text{anchor}} + m_{\text{bkg}} \cdot (qU - 17\,824.1\,\text{eV}) \tag{5.4}$$

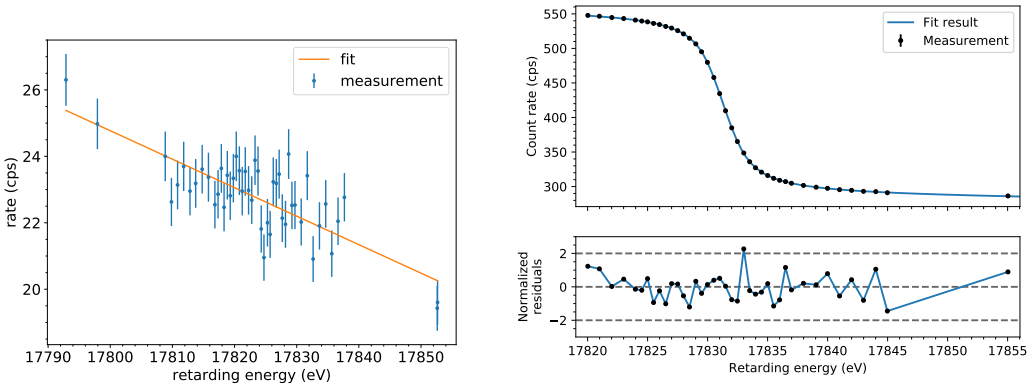

(a) (b)

Figure 5.2: (a) Rate vs retarding energy for pixel 0. The source was being pumped out, the magnetic field in the AP was set to $B_{\text{ana}} = 2.7\,\text{G}$. The fit indicates a linear slope of $m_{\text{bkg}} = (-0.086 \pm 0.010)\,\text{cps}\,\text{eV}^{-1}$. (b) Exemplary fit of the K-32 line in the SAP setting for pixel 0 and 92 stacked scans. The residuals normalised to their corresponding statistical uncertainty show no apparent structure.

5.2.2 Data selection and quality

Before and after the KATRIN neutrino mass 3 (KNM3) campaign krypton measurements were performed in the SAP setting in addition to a reference measurement in a symmetric setting. Various retarding potentials close to the expected line position of 17 824.1 eV were measured in each scan (lasting about 0.5 h) alternating between up and down scans. The number of scans for the different settings is shown in table 5.1. Differences in the number of scans are to some extent compensated by the source activity which decreased between the two SAP measurements.

Before stacking the scans potentially time-dependent drifts of the parameters have been investigated. As the line width is later used extensively its stability is important. To this end, adjacent up and down scans are stacked and fitted using the model described in section 5.2.1. The fit range has been chosen to be 17 814.5 eV to 17 850.5 eV for the symmetric setting and 17 819.5 eV to 17 855.5 eV for the SAP setting to regard for potential depression in the SAP. Pixels that are not fully illuminated by the source due to misalignment are excluded (see table D.1 for KNM3). As fitting all active pixels individually for each pair of up and down scans is computationally expensive, they are grouped in pseudorings consisting of four rings each (see table D.2 for a pixelwise definition). Every pseudoring is then fitted individually with the krypton model explained in section 5.2.1 and five free fit parameters: (A, E_0, Γ, B_{anchor}, m_{bkg}).

Figure 5.3 shows the time evolution of the krypton line width Γ_{Kr} for each pseudoring and stacked pair of scans. The line width shows a slight radial pattern. No significant linear drifts have been observed. An overview of the fitted linear drifts is given in table 5.2 for

every measurement. This motivates stacking all the scans for each measurement (nominal, pre and post KNM3) to gain statistics allowing a more sophisticated analysis as described in section 5.2.3.

Table 5.1: Spent measurement time for krypton in terms of scans. Each scan has a duration of roughly half an hour.

measurement	scans
symmetric	32
SAP pre KNM3	94
SAP post KNM3	107

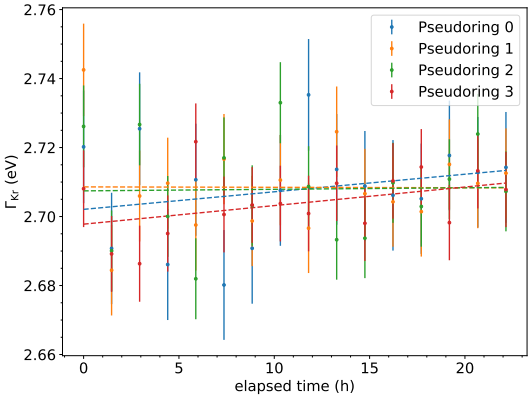

(a) symmetric

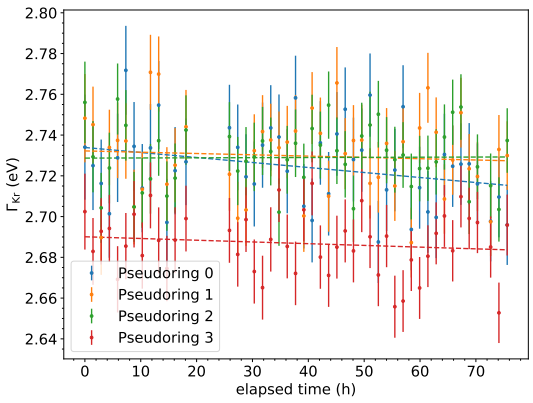

(b) SAP pre KNM3

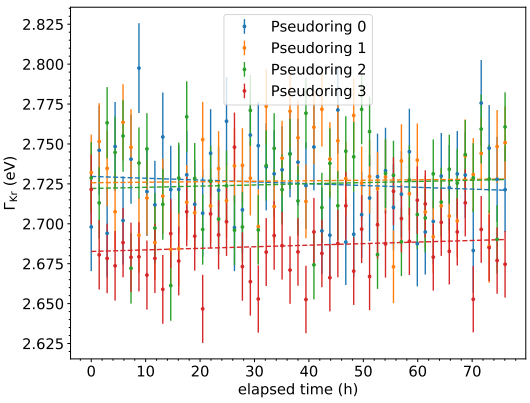

(c) SAP post KNM3

Figure 5.3: Time evolution of Γ_{Kr} for the three different measurements per pseudoring. Dashed lines show the fitted drifts to a linear order for each pseudoring.

5.2.3 Analysis strategy

As the magnetic field in the analysing plane affects the width of the transmission, which may translate into a broadened line width, extracting the magnetic fields for the SAP is done in a two step approach. Firstly the measurement performed in symmetric settings with $B_{\text{ana}} = 2.7\,\text{G}$ is fitted. This provides a very good energy resolution and little field inhomogeneities. The fit model and its free parameters are the same as in section 5.2.2. The background slope is left unconstrained in the fit. As the gaseous krypton in the WGTS may

Table 5.2: Fitted (linear) slope of the time evolution of Γ_{Kr} for the three different measurements (per pseudoring).

(a) symmetric

pseudoring	slope ($\mathrm{meV\,h^{-1}}$)
0	0.51 ± 0.59
1	-0.01 ± 0.48
2	0.04 ± 0.43
3	0.54 ± 0.40

(b) SAP pre KNM3

pseudoring	slope ($\mathrm{meV\,h^{-1}}$)
0	-0.25 ± 0.14
1	-0.06 ± 0.12
2	0.01 ± 0.11
3	-0.08 ± 0.10

(c) SAP post KNM3

pseudoring	slope ($\mathrm{meV\,h^{-1}}$)
0	-0.11 ± 0.17
1	0.03 ± 0.14
2	0.07 ± 0.13
3	0.10 ± 0.13

contain small amounts of residual tritium, the background slope is expected to be larger compared to the empty, pumped out source. Additionally the uncertainty on the magnetic field in the analysing plane of 1.75 % is taken into account via a MC propagation. Finally the line width Γ and its uncertainty can be extracted. This is then inserted via a pull-term in the fits of the SAP setting.

5.2.4 Results

In this section, the results of the krypton fits are presented. Instead of fitting B_{ana} directly, it is estimated using a profile likelihood. This is done for each FPD pixel separately. A similar analysis is performed for groups of pixels called patches. In the latter case however an additional parameter is profiled, hence 2D gridscans are obtained. The fits are judged using χ^2 as defined previously in eq. (2.13).

Pixelwise analysis

In order to estimate the magnetic field in the AP, for each pixel a profile likelihood of B_{ana} is performed: The spectrum is fitted multiple times for different values of the magnetic field B_{ana}. In each step, the fit minimises the χ^2 w.r.t. to the fit parameters given by the quintuplet (A, E_0, Γ, B_{anchor}, m_{bkg}). This leads to a profile as displayed for pixel 0 in fig. 5.4. The best fit value (orange) is at the minimum of an interpolated χ^2 using cubic spline interpolation (dashed) for a more precise result. The 1σ uncertainties are defined by $\Delta\chi^2 = 1$ and shown as a blue area. For further computations and comparisons the errors are symmetrized.
This profile likelihood procedure is repeated for all active pixels and gives a pixel map of the magnetic field and its uncertainty. Figure 5.5a shows that after 92 scans or roughly 40 h measurement time the relative (statistical) uncertainty on the magnetic field in the SAP is about 2 %. The goodness-of-fit is depicted in fig. 5.5b in terms of the reduced χ^2 for 35 degrees of freedom. There is no wise pattern visible that would indicate bad model assumptions e.g. for outer pixels. Moreover the χ^2 distribution (see also appendix B.3) is displayed in fig. 5.6. It shows a shift of the fits to larger χ^2 values compared to the expected distribution. This

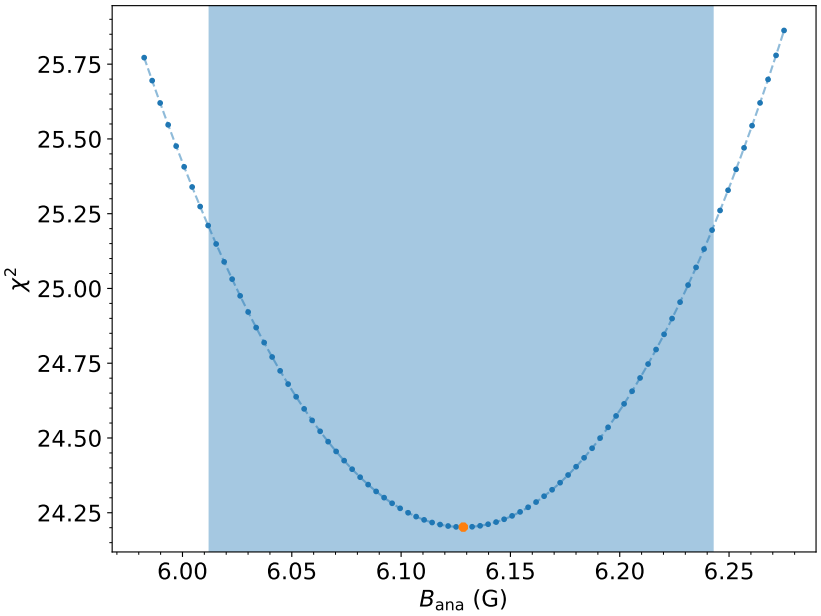

Figure 5.4: Profile likelihood of pixel 0. The dashed line corresponds to a cubic spline interpolation. The best fit is shown in orange, the 1σ uncertainty is indicated by the blue area.

may hint to not fully understood systematic uncertainties. Further analysis is needed to get a better agreement.
In general the pixelwise analysis allows for an extraction of the magnetic field in the analysing plane. This results can then be compared to simulations and potentially lead to a better understanding of the magnetic fields in the SAP setting. However in the neutrino mass analysis a pixelwise approach is not desirable as the computational effort to fit a tritium spectrum with pixelwise parameters but a shared neutrino mass is rather large. In order to regard inhomogeneities of the fields on the one hand but limit the computation time on the other hand, pixels with similar transmission properties are grouped together. This motivates the use of patches as described in the following section.

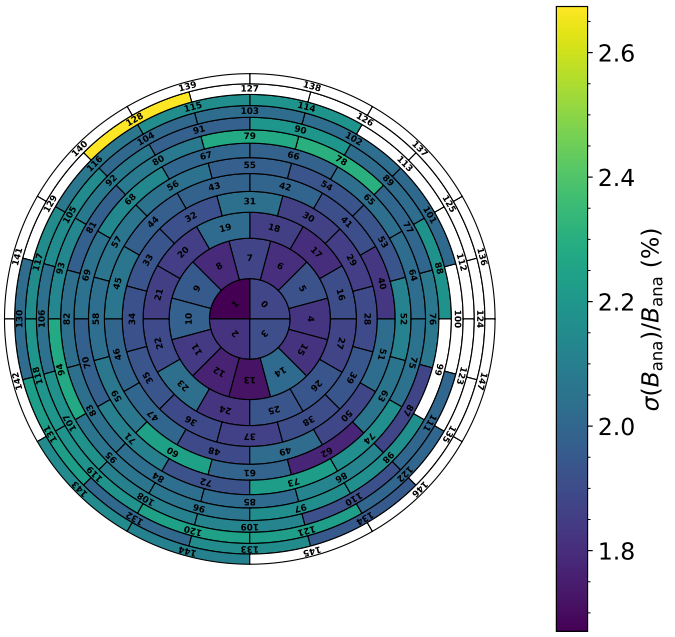

(a) Relative uncertainty on B_{ana}.

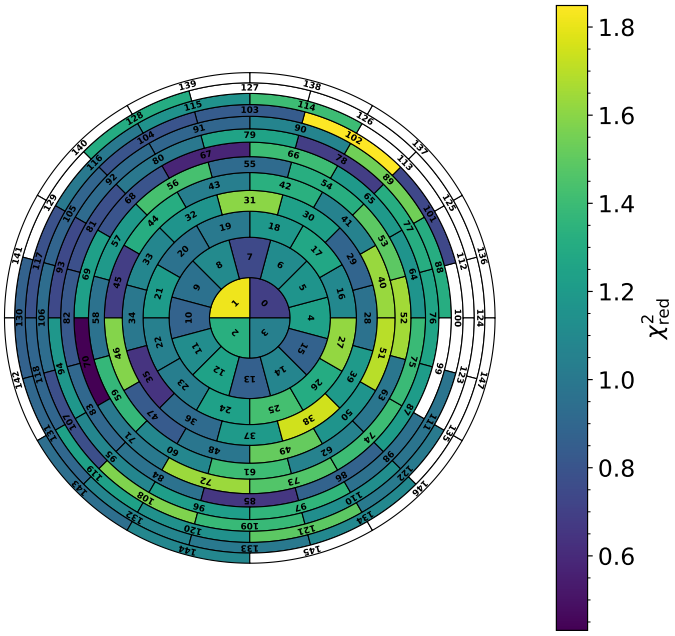

(b) χ^2_{red} for 35 degrees of freedom.

Figure 5.5: (a) Relative uncertainty on the fitted magnetic field in the SAP. The mean relative uncertainty is $(2.0 \pm 0.2)\,\%$. (b) χ^2_{red} (at 35 degrees of freedom) indicating good fits for all pixels and no apparent structure.

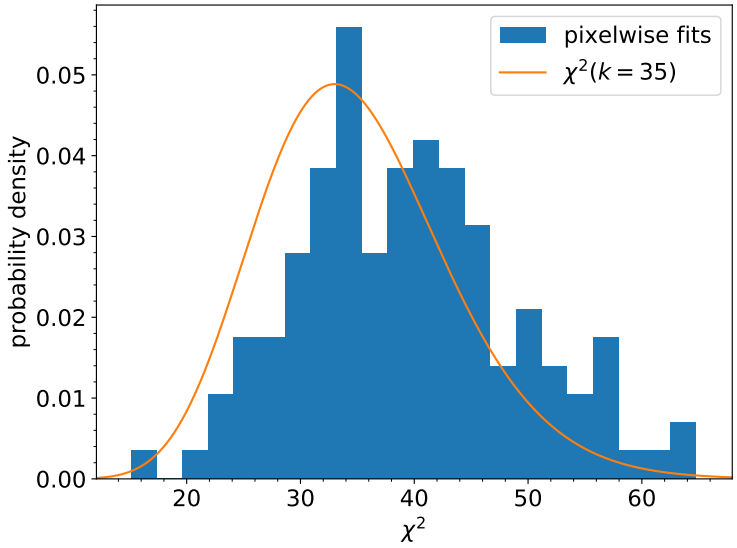

Figure 5.6: χ^2 distribution (35 degrees of freedom) for the pixelwise fits. Additionally the expectation for $k = 35$ degrees of freedom is shown.

Patchwise analysis

Fitting individual pixels is computationally expensive hence usually not performed in the neutrino mass analysis. If the magnetic field in the analysing plane is homogenous, the transmission function can be averaged for all pixels and subsequently the pixels can be combined. This allows for a fast fit of the spectrum. However in the case of a SAP the introduced inhomogeneities would broaden the transmission function as sketched in fig. 5.7a for a Gaussian spread of the magnetic field B_{ana}. Such a broadened transmission would worsen the energy resolution and therefore also the neutrino mass sensitivity. A countermeasure is to group pixels with similar transmission probabilities in patches as a compromise between computation time and energy resolution. This was done by Alexey Lokhov and Christian Weinheimer using the energy at half transmission. The obtained patches are displayed in fig. 5.7b and given explicitly in table D.3.
For the patchwise analysis the fitrange is more restricted. It is defined to be 17 818.5 eV to 17 850.5 eV for the symmetric setting and 17 823.5 eV to 17 855.5 eV for the SAP setting. Previously the residuals for subscans below these regions were larger, so for the moment those subscans are excluded.

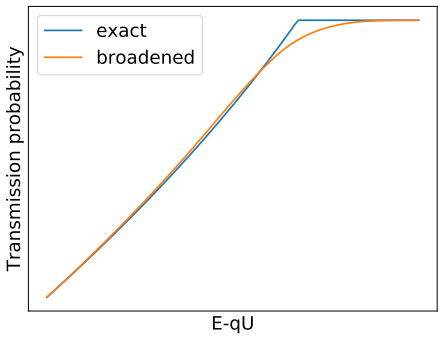

(a)

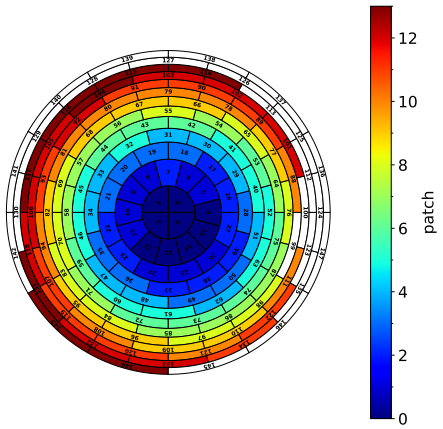

(b)

Figure 5.7: (a) Sketch of a broadened transmission due to a spread of the magnetic field in the AP. Exact refers to a transmission function with fixed B_{ana} while broadened is the average transmission function for a Gaussian distributed B_{ana}. (b) Patches for the SAP. White pixels are excluded. See also table D.3.

As each patch consists of multiple pixels, the statistics are larger compared to fitting pixels individually. Therefore instead of a one dimensional profile likelihood as in fig. 5.4 a two dimensional approach is preferred. In addition to the magnetic field B_{ana}, a generic broadening σ^2_{broad} is included. This broadening defines a Gaussian distribution that is convolved with the transmission function. In order to avoid a bias on σ^2_{broad}, the model is extended to the region $\sigma^2_{\text{broad}} < 0$ following the approach of [26]. Just as for the 1D profile likelihood, B_{ana} is varied and for each value χ^2 is minimised w.r.t. the same parameters (the quintuplet) as before. In the same way σ^2_{broad} is profiled for each given B_{ana}. This results in a 2D χ^2 map of both parameters as shown in fig. 5.8 for patch 0. The best fit is estimated as the minimum of the interpolated χ^2 using 2D cubic splines. A high anti-correlation between the two parameters is indicated by the 1σ ellipse. Figure 5.9a shows the χ^2_{red} for all patches at 30 degrees of

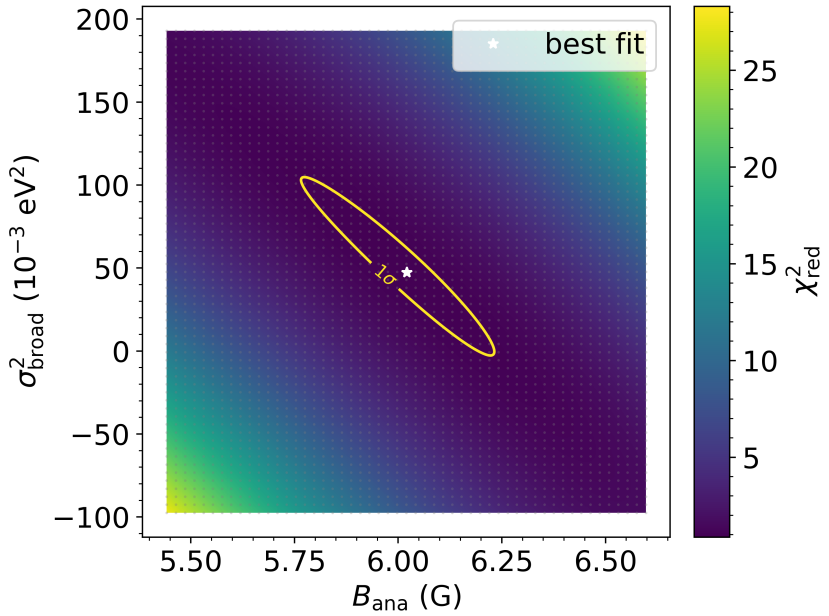

Figure 5.8: 2D profile likelihood for patch 0. Besides the best fit, its 1σ uncertainty ellipse is shown indicating high anti-correlation between the two parameters. 2D cubic splines have been used to interpolate between the grid points shown in grey.

freedom. The mean value indicated as dashed line shows good fits, with the post KNM3 being slightly better. Most likely this is due to the larger stabilisation time of the krypton source. Furthermore the high anti-correlation between B_{ana} and σ^2_{broad} depicted in fig. 5.9b is present for all patches. Its mean value (dashed) is about -0.96. This anti-correlation is expected as both parameters are related to the width of the transmission function.
Figure 5.10a shows the magnetic field in the analysing plane for the different patches. It decreases for the outer patches and is mostly in good agreement between the two measurements. Outliers are compensated by σ^2_{broad} shown in fig. 5.10b.

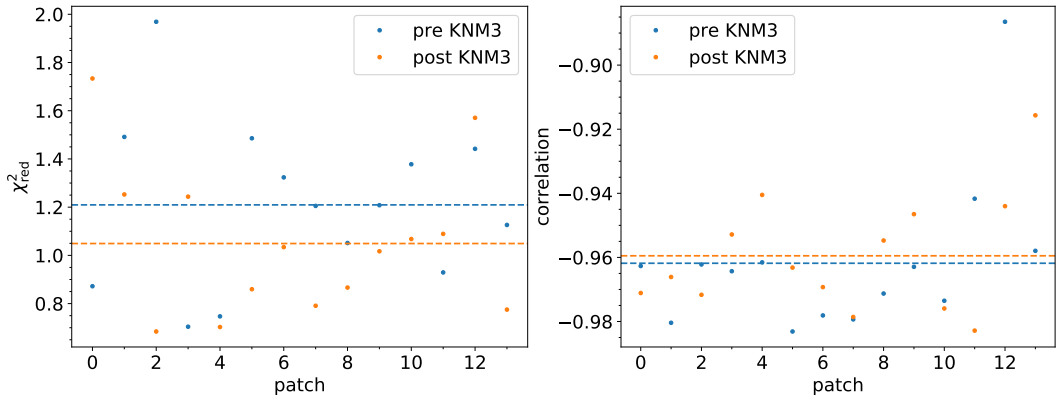

(a) (b)

Figure 5.9: (a) χ^2_{red} (at 30 degrees of freedom) for the two measurements. The post KNM3 measurement was taken after a longer time in which the krypton source could stabilise. The lower $\langle\chi^2_{\text{red}}\rangle$ (dashed) could be a hint to a more stable source. (b) Correlations between B_{ana} and σ^2_{broad}. For both measurements the mean (dashed) is about -0.96 indicating a high anti-correlation for all patches. This is expected as B_{ana} and σ^2_{broad} both are related to the width of the transmission function.

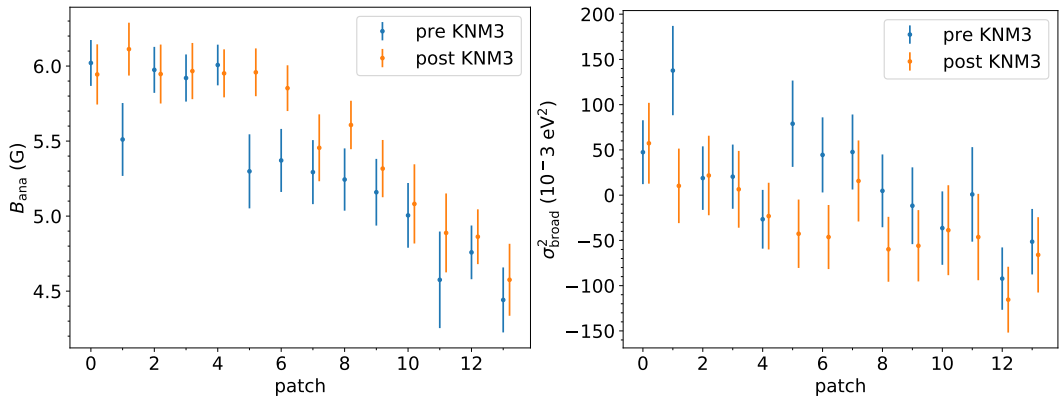

(a) (b)

Figure 5.10: (a) Magnetic field in the AP for all patches. For better readability the post KNM3 points are shifted w.r.t. their patch number. The decrease for outer patches is clearly visible. While most of the patches agree within their uncertainty there are a few outliers. In each case this is compensated by the highly anti-correlated broadening shown in (b). (b) Broadening for all patches. Similar to (a) the post KNM3 points are shifted for better readability. The agreement is quite good, while a few outliers are observed. This is the compensation of the magnetic field as stated previously.

5.3 Effects on KATRIN sensitivity

Precise knowledge of the magnetic fields in the AP is crucial for the neutrino mass sensitivity. Using the results described in section 5.2.4 allows to estimate the sensitivity using MC propagation within Fitrium. This is done for the patchwise analysis as this is likely to be used in the tritium analysis. Not only the uncertainties on B_{ana} and σ^2_{broad} are taken as an input but also their correlation.
Figure 5.11 shows that these parameter correlations have a large impact. The m_ν^2 distribution is much narrower if anti-correlations (here assumed to be -0.97 for all patches) are taken into account. As both parameters modify the transmission function in a similar way, they may cancel each other. However this effect is very large and may be exaggerated. Considering that an uncertainty on the magnetic field in the analysing plane affects all pixels or patches in the same way, varying the field in the AP and the broadening variance individually per patch may not be appropriate. Therefore additional correlations between the patches are introduced (not to be confused with parameter correlations).
Figure 5.12 shows the difference between fully correlated and individual patches in the MC propagation. The fully correlated approach (orange) has an uncertainty similar to a normal setting with a central analysing plane (green). It is certain that ignoring the correlations between patches hence underestimates the effect on the neutrino mass sensitivity. This result would suggest that instead of treating the patches individually a more accurate approach requires a shared propagation of uncertainties of the magnetic field. This would naturally give rise to correlations between patches. Due to statistically independence of these patches their correlation is not necessarily 1. However estimating this correlation a posteriori may be difficult and is beyond the scope of this thesis.

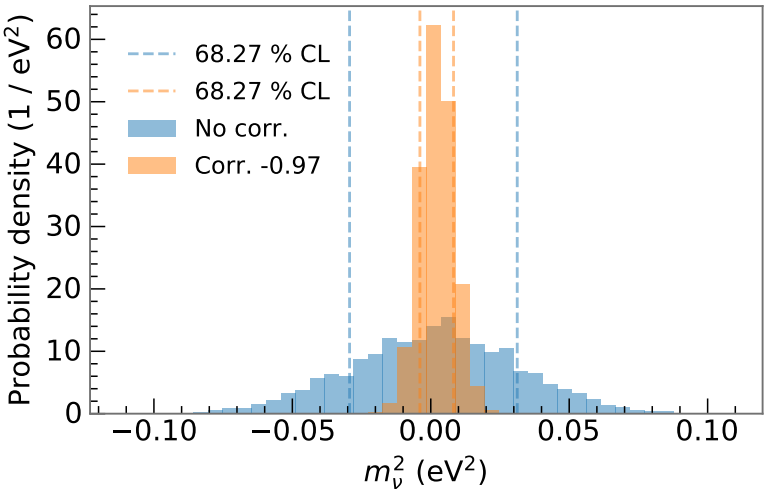

Figure 5.11: Effect of parameter correlation on m_ν^2. Plot and study by Christian Karl.

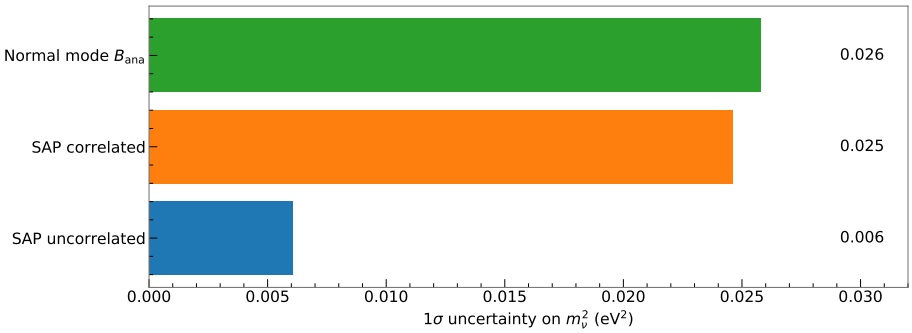

Figure 5.12: Effect of patchwise correlation on m_ν^2. Plot and study by Christian Karl.

Chapter 6

Conclusion and outlook

In this thesis a data-driven Monte Carlo simulation for the background in the KATRIN experiment has been developed. Using existing background measurements at elevated pressure as an input provided the possibility for a time- and event-based simulation of background processes in the main spectrometer. In general the non-Poisson (NP) character of the background could be reproduced successfully.
The time-correlated NP background shows a clear dependence on the underlying time binning. Shorter time bins in the form of subscans allow for a reduction of the NP fraction as events induced by nuclear decays spread over multiple subscans. However this leads to a correlation of different subscans as they cease to be fully independent.
Two background scenarios have been investigated. A worst case scenario allowing to study the NP background extensively has shown that induced correlations are indeed visible. Furthermore these correlations can be reduced by scanning faster or randomly instead of up and down w.r.t the retarding potentials.
Using a covariance matrix approach the impact of a NP background in a realistic scenario has been studied. While scanning randomly or faster showed significant improvements for a well pronounced NP background this does not hold in a more realistic case. Moreover the NP fraction can be described with a single number neglecting correlations of subruns without any substantial error.
In general the background can be reduced by a factor of 2 using a shifted analysing plane (SAP). As this introduces inhomogeneities in the electric and magnetic fields, precise field calibration measurements are necessary. In the framework of this thesis gaseous ^{83m}Kr that has been inserted into the windowless gaseous tritium source serves as the calibration tool. The mono-energetic K-32 conversion line is used to measure the magnetic field variation in the SAP. The analysis follows a two step approach. Firstly the reference line width is determined in the symmetric setting and afterwards the magnetic fields are extracted for the asymmetric SAP setting.
This is done for pixels and patches separately and provided a pixel map of the magnetic field to compare to simulations. Furthermore the patchwise analysis has shown a high correlation between the magnetic field in the AP and a generic Gaussian broadening of the transmission function. This correlation is of particular interest as it changes the impact of the field uncertainties on the neutrino mass sensitivity.
Finally it could be seen that a individual treatment of pixels or patches may not be suitable when propagating uncertainties into the neutrino mass. As in this approach correlations between the patches are neglected the impact can be overestimated. This has to be corrected by introducing correlations between those patches. However as they are statistically independent the exact correlation can only by deduced by the data itself which requires further investigations and a modification of the analysis strategy.

In summary this thesis provided insights in the NP background, its impact on the neutrino mass sensitivity and the effectiveness of possible countermeasures. Moreover the SAP has the potential to improve the neutrino mass sensitivity as it successfully decreases the background. Despite more thorough investigations needed for a robust and precise quantification of this improvement, first input values of the magnetic fields are provided to use in the third neutrino mass measurement campaign of KATRIN.

Bibliography

[1] J. Chadwick, "Intensitätsverteilung im magnetischen Spectrum der β-Strahlen von radium B + C," *Verhandl. Dtsc. Phys. Ges.* **16** (1914) 383. http://cds.cern.ch/record/262756.

[2] W. Pauli, "Offener Brief an die Gruppe der Radioaktiven bei der Gauvereins-Tagung zu Tübingen," 12, 1930. http://cds.cern.ch/record/83282/.

[3] E. Fermi, "Versuch einer Theorie der β-Strahlen. I," *Zeitschrift für Physik* **88** (1934) 161–177.

[4] C. Cowan, F. Reines, F. Harrison, H. Kruse, and A. McGuire, "Detection of the free neutrino: A Confirmation," *Science* **124** (1956) 103–104.

[5] F. Reines, C. L. Cowan, F. B. Harrison, and D. S. Carter, "Detection of neutrons with a large liquid scintillation counter," *Review of Scientific Instruments* **25** no. 11, (1954) 1061–1070.

[6] A. Bettini, *Introduction to Elementary Particle Physics.* Cambridge University Press, 2008.

[7] B. Povh *et al.*, *Teilchen und Kerne.* Springer Spektrum, Berlin, Heidelberg, 2014.

[8] R. Davis, D. S. Harmer, and K. C. Hoffman, "Search for neutrinos from the sun," *Phys. Rev. Lett.* **20** (May, 1968) 1205–1209.

[9] **Super-Kamiokande** Collaboration, Y. Fukuda *et al.*, "Evidence for oscillation of atmospheric neutrinos," *Phys. Rev. Lett.* **81** (Aug., 1998) 1562–1567.

[10] **Particle Data Group** Collaboration, P. A. Zyla *et al.*, "Review of Particle Physics," *Prog. Theor. Exp. Phys.* **2020** (2020) . 083C01.

[11] C. Kraus *et al.*, "Final results from phase II of the Mainz neutrino mass search in tritium beta decay," *Eur. Phys. J. C* **40** (2005) 447–468, arXiv:hep-ex/0412056.

[12] **Troitsk** Collaboration, V. Aseev *et al.*, "An upper limit on electron antineutrino mass from Troitsk experiment," *Phys. Rev. D* **84** (2011) 112003, arXiv:1108.5034 [hep-ex].

[13] KATRIN Collaboration and KATRIN Collaboration, "KATRIN design report 2004," tech. rep., Forschungszentrum, Karlsruhe, 2005. 51.54.01; LK 01.

[14] C. Karl, "Analysis of first tritium data of the KATRIN experiment," Master's thesis, Technische Universität München, 2018. https://www.katrin.kit.edu/publikationen/mth-karl.pdf.

[15] M. Kleesiek *et al.*, "β-decay spectrum, response function and statistical model for neutrino mass measurements with the katrin experiment," *The European physical journal / C* **79** no. 3, (2019) Article: 2014. 51.03.01; LK 01.

[16] K. M. Altenmüller, *Search for sterile neutrinos in beta decays.* Dissertation, Technische Universität München, München, 2019. http://nbn-resolving.de/urn/resolver.pl?urn:nbn:de:bvb:91-diss-20191010-1506307-1-4.

[17] J. Behrens *et al.*, "A pulsed, mono-energetic and angular-selective UV photo-electron source for the commissioning of the KATRIN experiment," *Eur. Phys. J. C* **77** no. 6, (2017) 410, arXiv:1703.05272 [physics.ins-det].

[18] M. Arenz *et al.*, "First transmission of electrons and ions through the KATRIN beamline," *Journal of Instrumentation* **13** no. 04, (Apr., 2018) P04020–P04020.

[19] **KATRIN** Collaboration, M. Aker *et al.*, "Improved upper limit on the neutrino mass from a direct kinematic method by KATRIN," *Phys. Rev. Lett.* **123** no. 22, (2019) 221802, arXiv:1909.06048 [hep-ex].

[20] A. K. Schaller, *Characterization and mitigation of the background in KATRIN.* Dissertation, Technische Universität München, München, 2020.

[21] F. Fränkle and D. Hinz, "Radon background measurements with increased spectrometer pressure." Electronic logbook, Feb., 2019. https://ikp-neu-katrin.ikp.kit.edu/elog/KNM1/3.

[22] P. Young, "Everything you wanted to know about data analysis and fitting but were afraid to ask," 2012. https://arxiv.org/abs/1210.3781v3.

[23] S. Mertens, *Study of Background Processes in the Electrostatic Spectrometers of the KATRIN Experiment.* PhD thesis, Karlsruhe Institute of Technology, 2012.

[24] A. Lokhov, F. Fränkle, L. Schlüter, T. Thuemmler, and D. Hinz, "Background measurements." Electronic logbook, Dec., 2019. https://ikp-neu-katrin.ikp.kit.edu/elog/KNM2/165.

[25] K. Altenmüller *et al.*, "High-resolution spectroscopy of gaseous 83m kr conversion electrons with the KATRIN experiment," *Journal of Physics G: Nuclear and Particle Physics* **47** no. 6, (May, 2020) 065002.

[26] A. Belesev *et al.*, "Investigation of space-charge effects in gaseous tritium as a source of distortions of the beta spectrum observed in the Troitsk neutrino-mass experiment," *Phys. Atom. Nucl.* **71** (2008) 427–436.

[27] A. M. Mathai and H. J. Haubold, *Probability and Statistics.* De Gruyter, Berlin, Boston, 2018.

Appendix A

Acronyms

AP analysing plane 6

BKG1 background dataset 1 20

BKG2 background dataset 2 27

C.L. confidence level 5

CPS cryogenic pumping section 10

DPS differential pumping section 10

FPD focal plane detector 10

IE inner electrode 11

KATRIN Karlsruhe Tritium Neutrino 5

KNM1 KATRIN neutrino mass 1 11

KNM2 KATRIN neutrino mass 2 27

KNM3 KATRIN neutrino mass 3 37

cps counts per second 18

MAC-E filter magnetic adiabatic collimation combined with an electrostatic filter . . 6

MC Monte Carlo 8

MS main spectrometer 10

MTD measurement time distribution 25

NEG non-evaporable getter 16

NP non-Poisson 12

PAE post-acceleration electrode 11

PS pre-spectrometer 10

RW rear wall 9

SAP shifted analysing plane 35

SM standard model 1

WGTS windowless gaseous tritium source 10

Appendix B

Probabilities and statistics

In the following, a short overview of important probability distributions and other statistical measures will be given.

B.1 Poisson distribution

The Poisson distribution is valid for processes consisting of independent events and can be derived as a limit using a binomial probability law. Its probability density is given by

$$p(x) = \begin{cases} \frac{\lambda^x e^{-\lambda}}{x!}, & \text{if } x \in \mathbb{N} \\ 0, & \text{otherwise} \end{cases} \tag{B.1}$$

with mean λ and standard deviation $\sqrt{\lambda}$ [27].

B.2 Normal distribution

The normal or Gaussian distribution is the most common probability distribution. Its probability density is given by

$$p(x) = \frac{1}{\sqrt{2\pi}\sigma} \cdot e^{\frac{(x-\mu)^2}{2\sigma^2}} \tag{B.2}$$

with mean μ and standard deviation σ [27].

B.3 χ^2 distribution

The χ^2 distribution is widely used when it comes to hypothesis testing, regression tasks or model building. It is defined as

$$p(x) = \begin{cases} \frac{1}{2^{\frac{k}{2}}\Gamma(\frac{k}{2})} x^{\frac{k}{2}-1} e^{-\frac{x}{2}}, & \text{for } k \in \mathbb{N} \\ 0, & \text{otherwise} \end{cases} \tag{B.3}$$

with k denoting the degrees of freedom and Γ being the usual gamma function. Its mean is given by k [27].

Appendix C

Parameters of generated Asimov spectra

In the following, additional simulation parameters used for the generation of Asimov spectra are given.

Table C.1: Parameters of generated tritium spectra

parameter	value	
$\epsilon_{\mathrm{detector}}$	0.95	
ρd	4.2×10^{21}	m^{-2}
B_{S}	2.52	T
B_{ana}	6.3	G
B_{max}	4.2	T
m_ν^2	0.0	eV^2
E_0	18 575.0	eV
N	1	
T	30	K

Appendix D

Data preselection and patches

Table D.1: Excluded FPD pixels.

measurement phase	excluded pixels
KNM1	97, 98, 99, 110, 111, 121, 122, 139, 140, 141, 142
KNM2	97, 98, 110, 111, 121, 122, 100, 112, 113, 123, 124, 125, 126, 127, 128, 129, 130, 134, 135, 136, 137, 138, 139, 140, 141, 142, 143, 144, 145, 146, 147
KNM3	99, 100, 112, 113, 123, 124, 125, 126, 127, 128, 129, 130, 135, 136, 137, 138, 139, 140, 141, 142, 145, 146, 147

Table D.2: Definition of pseudorings.

pseudoring	pixel
0	0-27
1	28-63
2	64-99
3	100-147

Table D.3: Definition of patches for SAP.

patch	pixel
0	0, 1, 2, 3, 4, 12, 13, 14, 15
1	5, 6, 8, 9, 10, 11, 24, 25, 26
2	7, 16, 17, 22, 23, 27, 37, 38, 39
3	18, 19, 20, 21, 28, 35, 36, 49, 50
4	29, 30, 31, 33, 34, 47, 48, 51, 62
5	32, 40, 41, 45, 46, 52, 60, 61, 63
6	42, 43, 44, 53, 59, 72, 73, 74, 75
7	54, 56, 57, 58, 64, 71, 85, 86, 87
8	55, 65, 69, 70, 76, 83, 84, 97, 98
9	66, 67, 68, 77, 82, 95, 96, 109, 110
10	78, 79, 80, 81, 88, 94, 108, 111, 121
11	89, 90, 91, 93, 107, 119, 120, 122, 134
12	92, 101, 102, 103, 105, 106, 118, 132, 133
13	104, 114, 115, 116, 117, 131, 143, 144

List of Figures

List of Tables

Selbstständigkeitserklärung

Hiermit erkläre ich, die vorliegende Arbeit mit dem Titel

Time-correlated Background and Background Mitigation Strategies in the KATRIN Experiment

selbständig verfasst zu haben und keine anderen als die angegebenen Quellen und Hilfsmittel verwendet zu haben.

München, den 13. Oktober 2020

Alessandro Schwemmer